Institut für Physikalische und Theoretische Chemie,

Lehrstuhl für Theoretische Chemie
der Technischen Universität München

Modeling of ultrafast electron-transfer processes: multi-level Redfield theory and beyond

Dassia Egorova

Vollständiger Abdruck der von der Fakultät für Chemie der Technischen Universität München zur Erlangung des akademischen Grades eines

Doktors der Naturwissenschaften

genehmigten Dissertation.

Vorsitzender:	Univ.-Prof. (Komm.) Dr. W. Nitsch, em.
Prüfer der Dissertation:	1. Univ.-Prof. Dr. W. Domcke
	2. Univ.-Prof. Dr. S. F. Fischer

Die Dissertation wurde am 07.11.2002 bei der Technischen Universität München eingereicht und durch die Fakultät für Chemie am 13.01.2003 angenommen.

To my mother

CONTENTS

1. INTRODUCTION

Being a fundamental phenomenon in chemistry, physics and biology, electron transfer (ET) has been attracting enormous attention of both experimentalists and theoreticians for many years. First observations of condensed-phase ET processes were made already in the nineteenth century by Davy [1] and Weyl [2]. As for the modern era of ET studies, it is believed to begin after the second World War.

Theoretical developments in the description of ET processes start with the idea of Franck (1949) and Libby (1952) [3] that ET reaction rates are determined by "horizontal Franck-Condon factors". In 1956, Marcus proposed the first quantitative theory of ET in solution, based on the calculation of the Franck-Condon factor in the classical limit [4], while in 1959 Levich and Dogonadze advanced the incorporation of quantum effects in the ET-rate expression [5]. In 1974, Kestner, Logan and Jortner developed a quantitative description of ET processes in terms of radiationless transitions [6], proposing a microscopic ET rate expression based on the Fermi Golden Rule formula [7], which implies a perturbative treatment of the nonadiabatic coupling between initial (donor) and final (acceptor) electronic states and is valid for so-called nonadiabatic ET processes. The theoretical description of nonadiabatic ET reactions found further development in the works of Bixon and Jortner, who included effects of solvation dynamics in the rate expression [8], and of Sumi and Marcus, who proposed a partitioning of the reaction coordinate in vibrational and solvent parts, which results in a solvent-coordinate dependent ET rate expression by the assumption of fast relaxation in the nuclear coordinate [9].

In recent years, the attention has shifted towards photoinduced ET reactions occurring at subpicosecond time scales, so-called ultrafast ET processes [10]. Extensive experimental investigations of ET in the femtosecond regime have been performed, e.g., by Barbara and coworkers for betaines [11–15] and mixed valence compounds [16–19], and by Yoshihara and collaborators for various intermolecular reactions [20–24]. Observations of ultrafast ET processes also have been reported for bacterial photosynthetic reaction centers [25, 26] and

in numerous other systems [27–34].

The femtosecond ET reactions occur much faster than the solvation of the surrounding medium, which implies that the ET dynamics is controlled by high-frequency intramolecular modes rather than by the solvent relaxation (as it is assumed in the traditional rate descriptions). Observations of quantum beats in time-resolved transient absorption or fluorescence signals [18, 19, 25, 27–29, 31, 32] reflect nonstationary wave-packet motion in underdamped vibrational modes, induced by fs laser excitation. This coherent vibrational motion may significantly affect the reaction process.

Obviously, a generalization of the theory of ET processes is required to describe ultrafast ET reactions. A number of methods have been developed to refine the nonadiabatic-ET rate expression. Coalson *et al.*, e.g., have extended the Golden-Rule formula to include effects of nonequilibrium nuclear distribution of the initially prepared state [35]. Barbara and coworkers have developed a hybrid model [13, 36] of the classical vibrational electron transfer theory of Sumi and Marcus and the vibronic electron transfer theory of Bixon and Jortner in order to rationalize their experimental results [13, 36]. It should be noted, however, that these approaches are still based on perturbation theory with respect to the ET coupling, and their validity may justifiably be questioned for ET processes in the femtosecond regime, which necessarily require strong electronic coupling.

Experimental evidence that ultrafast ET is not a simple rate process has motivated theoretical treatments, which do not aim at the determination of a certain reaction rate, but try to develop a nonperturbative quantum-mechanical description. Since a direct full quantum-mechanical treatment of the polyatomic ET system including the solvent environment is not possible, a reduced density-matrix description of open systems [37–39] has been adopted for the modeling of ultrafast ET in the condensed phase. This approach, which is not limited to small values of the electronic coupling, implies a separation of the problem into a relevant (system) and irrelevant (bath) parts. The idea is to treat only the few degrees of freedom of the system explicitly, while all the others are traced out, being regarded as a dissipative environment. The simplest and the most well-studied model which can be used for such

a description of ET consists of a two-level system interacting with a harmonic bath and is known as the spin-boson model [37, 40]. The two levels are normally referred to as donor and acceptor electronic states. For the case of linear coupling to a harmonic bath, a numerically exact solution can be obtained using the Feynman path-integral approach [41–44].

The observations of coherent oscillations have revealed the importance of vibrational motion as a driving force for ultrafast ET and the necessity of an explicit treatment of underdamped vibrational degrees of freedom. This can be achieved in the spin-boson frame by transforming the Hamiltonian to the reaction-mode representation [45, 46], where the dissipative system is represented by one or several harmonic modes coupled to two electronic states and to a bath of harmonic oscillators. The dynamics of the system modes is then treated exactly, while an approximate description for the bath modes (e.g., linear response theory) is used [47].

The observation of ultrafast ET reactions where only few intramolecular modes are strongly coupled to the ET, while all the others seem to be indirectly involved, justifies a perturbative treatment of the system-bath coupling. This strategy allows to avoid computationally expensive path-integral calculations and to simplify considerably the numerics. The reaction modes, coupled to the relevant electronic states, constitute the system, which is weakly interacting with a dissipative environment, representing all the other vibrational degrees of freedom. This approach was initialized by Jean *et al.* [48], who have proposed to adopt Redfield theory for relaxation [49], and by May *et al.* [50] and Wolfseder *et al.* [51, 52], who have advanced the so-called diabatic-damping model for the ET description.

Developed in the context of nuclear magnetic-resonance and being frequently applied to the two-state Spin-Boson problem, Redfield theory can be also formulated for the system Hamiltonian in the reaction-mode representation and is referred to as multi-level Redfield theory in this case [48, 53, 54]. The system-eigenstate representation is adopted for the reduced density matrix in this approach, which requires the diagonalization of the system Hamiltonian. This is the only principal numerical bottleneck of multi-level Redfield theory, which limits the number of modes in the system Hamiltonian.

The diabatic-damping model is similar to Redfield theory as it is also perturbative with respect to the system-bath interaction, but it is more approximate. The relaxation operator, derived by Takagahara *et al.* [46] for a damped harmonic mode in a system of uncoupled electronic states, is adopted in this approach. This implies the harmonic approximation for the reaction modes and the rotating-wave approximation [38] for the system-bath interaction operator, as well as the neglect of the nonadiabatic electronic coupling between donor and acceptor state in the dissipation description. The advantages of the diabatic-damping model are that the diagonalization of the system Hamiltonian is not required, and that the resulting Lindblad-form [55] of the relaxation operator allows the use of a numerically efficient Monte-Carlo propagation scheme [56].

The ability of multi-level Redfield theory to describe ET processes with arbitrary strength of the nonadiabatic electronic coupling as well as its computational efficiency have been pointed out in Refs. [48] and [53], where a single-mode system Hamiltonian has been employed. Afterwards, the approach has been also applied to model bridge-mediated long-range ET [57] and to analyze two-site two-mode ET processes [58].

Single- and multi-mode system-Hamiltonian model calculations have been performed within the diabatic-damping model for ultrafast ET in the inverted region [52, 59, 60], with emphasis on the importance of the vibrational wave-packet motion. The wave-packet dynamics has been also addressed in Ref. [50]. Recently, the accuracy of the diabatic-damping description for the models of Refs. [52, 59] has been investigated by comparison with multi-level Redfield theory [61]. The limitations of the diabatic-damping model and its possible improvement have also been discussed in Ref. [62].

In this work, we apply multi-level Redfield theory to model ultrafast ET processes in the normal and inverted regions. We focus on reactions exhibiting coherent wave-packet motion in the excited and/or ground electronic states. The Redfield-theory approach allows us to reveal the role of the vibrational motion in the ultrafast ET dynamics, as well as to monitor and follow the wave-packet evolution in the electronic states of interest.

Furthermore, we investigate the validity of the secular approximation to Redfield the-

ory and of the so-called stationary Redfield-tensor approximation for various ET models, providing a detailed analysis of the possible breakdown of these approximations.

The nonperturbative character of the Redfield-theory description of ET processes with respect to the electronic coupling allows to investigate the range of the validity of the conventional Golden-Rule approach. Employing the transformation of the Hamiltonian to the normal-mode form and evaluating the steepest-descent formula for the Golden-Rule rate, we compare Golden-Rule and Redfield-theory predictions for ET in the normal region and demonstrate the breakdown of the Golden-Rule formula with the increase of the electronic coupling.

The description of ET processes within the diabatic-damping model is reviewed and its validity is discussed by comparison with Redfield-theory calculations. The model is found to be very accurate for small to intermediate values of the electronic coupling in the considered examples. Not surprisingly, its results start to deviate from those of the Redfield theory with the further increase of the electronic-coupling strength.

Finally, the validity of Redfield theory itself (i.e., the validity of the perturbative treatment of the system-bath coupling) is considered by comparison with numerically exact results obtained with the self-consistent hybrid approach, developed by Wang *et al.* [63]. To our knowledge, the range of applicability of multi-level Redfield theory for ET processes has not yet been systematically investigated, although the Redfield-theory description of the two-state Spin-Boson system has been tested versus exact results by several groups [37, 64–66]. The quantitative analysis shows that the relevant physics of ET is reliably described by multi-level Redfield theory for a relatively large range of the system-bath coupling. As expected, the approach proves to be very accurate for a weak system-bath interaction, but it also performs reasonably well for larger values of the system-bath coupling at short time scales. It should be pointed out that the numerical effort of the Redfield-theory calculations (see Appendix B for details) is negligibly small compared to that of the exact calculations with the self-consistent hybrid approach. Even calculations with the time-dependent Redfield tensor, which are the most expensive, do not require more than a half an hour (for

the single-mode system Hamiltonian) on a single work station, while several days may be required to obtain converged results within the self-consistent hybrid approach.

Two and three electronic-state models with a single reaction mode are considered in this work, while a Redfield calculation with three system modes has been reported elsewhere [61]. The numerical propagation of the reduced density matrix for the times of interest allows us to monitor the time evolution of the expectation value of any system variable. The population dynamics of the relevant electronic states has been chosen as a suitable observable of the ET process. The wave-packets in these states are represented by the corresponding projection of the coordinate representation of the reduced density matrix.

Two electronic-state models serve to investigate ET driven by wave-packet motion in the initially excited donor state, as well as the validity of all the approximations, mentioned above, and of multi-level Redfield theory itself. Specific features of the system dissipative dynamics for various parameter sets, in particular for ET in the normal and inverted regions, are outlined.

Three electronic-state models are constructed in order to demonstrate the possibility of vibrational coherences in the ground state during a back-ET reaction [18, 32]. The back ET is supposed to occur via an intermediate dark state, which bridges the initially excited charge-transfer state and the ground state. It is shown that vibrational wave-packet motion in the excited state can be transferred back to the ground state during the ultrafast ET reaction. Furthermore, it is found that wave-packet motion in the ground state can be generated, even if no moving wave packet has been prepared in the initially excited state.

2. REDFIELD THEORY FOR OPEN QUANTUM SYSTEMS

Open or dissipative quantum systems have been a subject of intensive research since many decades [37]. Such systems are conventionally described in terms of the reduced density-matrix formalism, the corresponding equation of motion being obtained by means of a well-established projection technique [67, 68]. Redfield theory for dissipation, which was originally derived in the nuclear magnetic-resonance frame [49], is also based on the reduced density-matrix approach and implies the Born and Markov approximations in the relaxation description, which allow to explicitly trace out bath variables from the relaxation operator and to obtain a local-in-time equation of motion for the reduced density matrix.

2.1 Reduced density-matrix formalism

Generally, no meaningful wave function can be assigned to an open system, because of its irreversible dynamics. The latter, however, can be described in terms of a reduced density matrix. Let us briefly discuss the principal ideas of this description.

A density-matrix or density-operator description of an isolated system is analogous to that provided by a wave function, the density matrix (operator) being defined as

$$\rho(\mathbf{x},t) = |\Psi(\mathbf{x},t)\rangle\langle\Psi(\mathbf{x},t)|, \tag{1}$$

where $|\Psi(\mathbf{x},t)\rangle$ is the corresponding wave function and $\mathbf{x}$ is a complete coordinate set. It is straightforward to show that the expectation value of an isolated-system variable

$$A(t) = \langle\Psi(\mathbf{x},t)|\hat{A}(\mathbf{x})|\Psi(\mathbf{x},t)\rangle,$$

where $\hat{A}(\mathbf{x})$ is the corresponding operator, can be then also found as

$$A(t) = \mathrm{tr}\{\hat{A}(\mathbf{x})\rho(\mathbf{x},t)\}. \tag{2}$$

If one regards an open system as a subsystem of the isolated system, the coordinate set $\mathbf{x}$ would include the subsystem (open-system) degrees of freedom, $\mathbf{Q}$, and remaining degrees

of freedom, $\mathbf{q}$, which would constitute a dissipative environment for the open system and can be thus referred as a thermal bath or reservoir. Open-system variables depend only on the coordinate set $\mathbf{Q}$, which allows to determine the corresponding expectation values in analogy to eq. (2) as

$$a(t) = \mathrm{tr}\{\hat{a}(\mathbf{Q})\sigma(\mathbf{Q},t)\}, \tag{3}$$

where $\sigma(\mathbf{Q},t)$ is the reduced density matrix (operator), which, in turn, is obtained as

$$\sigma = \mathrm{tr}_B\{\rho\}, \tag{4}$$

the trace being taken over the bath degrees of freedom $\mathbf{q}$ (see, e.g., Ref. [39] or any textbook on quantum mechanics for details of the derivation of eqs. (3), (4)).

The time-development of the isolated-system density matrix ρ is determined by the Liouville-von-Neumann equation

$$\frac{\partial\rho}{\partial t} = -i[H,\rho] = -i\mathcal{L}\rho, \tag{5}$$

where $\mathcal{L}$ is a Liouville super-operator $\mathcal{L} = [H,]$ and H is the complete (isolated-system) Hamiltonian. The latter can be expressed as a sum of an open-system Hamiltonian, H_S, a bath Hamiltonian, H_B, and a system-bath interaction operator, H_{SB},

$$H = H_S + H_B + H_{SB}. \tag{6}$$

The same relation holds for the Liouville super-operators

$$\mathcal{L} = \mathcal{L}_S + \mathcal{L}_B + \mathcal{L}_{SB}. \tag{7}$$

The equation of motion for the reduced density matrix σ can be formally obtained from eqs. (4), (5) by a standard projection technique [67, 68]. Introducing a projection operator

$$P = \rho_B \mathrm{tr}_B,$$

where ρ_B is the equilibrium bath density matrix

$$\rho_B = \frac{e^{-H_B/kT}}{\mathrm{tr}_B\{e^{-H_B/kT}\}}, \tag{8}$$

we obtain the general master equation for the reduced density matrix [68]

$$\frac{\partial\sigma}{\partial t} = -i\mathcal{L}_S\sigma - \int_0^t d\tau\mathcal{G}(\tau)\sigma(t-\tau), \tag{9}$$

with

$$\mathcal{G}(\tau) = \mathrm{tr}_B\{\mathcal{L}_{SB}e^{-i\mathcal{L}(1-P)\tau}\mathcal{L}_{SB}\rho_B\}. \tag{10}$$

The initial condition

$$\rho(t=0) = \sigma(t=0)\rho_B(t=0)$$

and the thermal equilibrium of the bath, eq. (8), at $t = 0$ have been assumed in the derivation of eq. (9).

Obviously, the first term on the rhs of the master equation (9) describes the dynamics of the relevant system in the absence of dissipation. The last term on the rhs, with the kernel (10), accounts for the interaction with the bath and is usually referred to as a relaxation operator.

2.2 Redfield equation

The challenge of the reduced density-matrix (RDM) description of open systems is to solve the equation of motion (9) without explicit treatment of the bath degrees of freedom. Unfortunately, the exact solution of (9) is rarely possible[1], and a number of approximative methods have been developed [37, 69–71]. In Redfield theory, in particular, a perturbative treatment of the system-bath coupling (Born approximation) is implied. The expansion of the memory kernel (10) up to the second order in H_{SB}

$$\mathcal{G}(\tau) = \mathrm{tr}_B\{\mathcal{L}_{SB}e^{-i(\mathcal{L}_S+\mathcal{L}_B)\tau}\mathcal{L}_{SB}\rho_B\} \tag{11}$$

[1]Low-dimensional systems in harmonic dissipative environments, e.g., can be treated exactly within the path-integral methodology [37, 44].

allows to trace out the bath variables and to reduce the problem to the open-system dimension. Furthermore, a local-in-time equation for the RDM is obtained in the framework of Redfield theory, since the assumption of Markovian system dynamics

$$\sigma(t-\tau) \simeq e^{i\mathcal{L}_S\tau}\sigma(t), \tag{12}$$

is implied in the perturbative treatment of the system-bath coupling (i.e., if only terms up to the second order in H_{SB} are retained)[2].

Hence, the Redfield equation for the RDM is obtained by substitution of eqs. (11) and (12) in eq. (9)

$$\frac{\partial\sigma}{\partial t} = -i[H_S,\sigma] + \mathcal{R}(\sigma), \tag{13}$$

where

$$\mathcal{R}(\sigma) = -\int_0^t d\tau \mathrm{tr}_B\{[H_{SB},[H_{SB}(\tau),\sigma(t)\rho_B]]\} \tag{14}$$

is the Redfield relaxation operator and

$$H_{SB}(\tau) = e^{-i(H_S+H_B)\tau}H_{SB}e^{i(H_S+H_B)\tau}. \tag{15}$$

The Redfield equation was originally written in the system-eigenstate representation [49]

$$\frac{\partial\sigma_{\mu\nu}(t)}{\partial t} = -i\omega_{\mu\nu}\sigma_{\mu\nu}(t) + \sum_{\kappa\lambda} R_{\mu\nu\kappa\lambda}\sigma_{\kappa\lambda}(t), \tag{16}$$

with the basis states defined via

$$H_S|\mu\rangle = E_\mu|\mu\rangle, \tag{17}$$

so that $\sigma_{\mu\nu} = \langle\mu|\sigma|\nu\rangle$ and $\omega_{\mu\nu} = E_\mu - E_\nu$. The last term in eq. (16) is obtained as

$$\sum_{\kappa\lambda} R_{\mu\nu\kappa\lambda}\sigma_{\kappa\lambda}(t) = \langle\mu|\mathcal{R}(\sigma)|\nu\rangle,$$

[2]It is noted, though, that there is a number of methods developed, which take into account non-Markovian effects (see, e.g., [72, 73] and references therein).

and the relaxation is described by the Redfield tensor $R_{\mu\nu\kappa\lambda}$, which is usually written as a sum

$$R_{\mu\nu\kappa\lambda} = \Gamma^{+}_{\lambda\nu\mu\kappa} + \Gamma^{-}_{\lambda\nu\mu\kappa} - \delta_{\nu\lambda}\sum_{\alpha}\Gamma^{+}_{\mu\alpha\alpha\kappa} - \delta_{\mu\kappa}\sum_{\alpha}\Gamma^{-}_{\lambda\alpha\alpha\nu}, \tag{18}$$

with

$$\begin{aligned}\Gamma^{+}_{\lambda\nu\mu\kappa} &= \int_0^t d\tau \left\langle \langle\lambda|H_{SB}|\nu\rangle\langle\mu|\tilde{H}_{SB}(\tau)|\kappa\rangle\} \right\rangle_B e^{-i\omega_{\mu\kappa}\tau} \\ \Gamma^{-}_{\lambda\nu\mu\kappa} &= \int_0^t d\tau \left\langle \langle\lambda|\tilde{H}_{SB}(\tau)|\nu\rangle\langle\mu|H_{SB}|\kappa\rangle \right\rangle_B e^{-i\omega_{\lambda\nu}\tau}.\end{aligned} \tag{19}$$

Here, we have introduced the notation

$$\tilde{H}_{SB}(\tau) = e^{-iH_B\tau}H_{SB}e^{iH_B\tau},$$

and $\langle ... \rangle_B$ denotes a thermal averaging over the bath,

$$\left\langle \langle\lambda|H_{SB}|\nu\rangle\langle\mu|\tilde{H}_{SB}(\tau)|\kappa\rangle \right\rangle_B = \mathrm{tr}_B\{\langle\lambda|H_{SB}|\nu\rangle\langle\mu|\tilde{H}_{SB}(\tau)|\kappa\rangle\rho_B\}.$$

In many applications the system-bath interaction operator, H_{SB}, can be factorized, i.e., written as a sum of products

$$H_{SB} = \sum_k Q_k F_k \tag{20}$$

of system, Q_k, and bath, F_k, operators. In this case, the relaxation operator (14) reads

$$\mathcal{R}(\sigma) = \sum_{kl}\int_0^t d\tau\{[Q_k, Q_l(\tau)\sigma(t)]\,\langle F_k F_l(\tau)\rangle_B - [Q_l, \sigma(t)Q_k(\tau)]\,\langle F_k(\tau)F_l\rangle_B\} \tag{21}$$

where

$$Q_k(\tau) = e^{-iH_S\tau}Q_k e^{iH_S\tau}, \quad F_k(\tau) = e^{-iH_B\tau}F_k e^{iH_B\tau},$$

and the Redfield-tensor components are given by

$$\begin{aligned}\Gamma^{+}_{\lambda\nu\mu\kappa} &= \sum_{kl}\langle\lambda|Q_k|\nu\rangle\langle\mu|Q_l|\kappa\rangle\int_0^t d\tau\,\langle F_k F_l(\tau)\rangle_B\, e^{-i\omega_{\mu\kappa}\tau} \\ \Gamma^{-}_{\lambda\nu\mu\kappa} &= \sum_{kl}\langle\lambda|Q_k|\nu\rangle\langle\mu|Q_l|\kappa\rangle\int_0^t d\tau\,\langle F_k(\tau)F_l\rangle_B\, e^{-i\omega_{\lambda\nu}\tau}.\end{aligned} \tag{22}$$

The only bath-dependent factors in eqs. (21), (22) are bath correlation functions $\langle F_k F_l(\tau)\rangle_B$ and $\langle F_k(\tau)F_l\rangle_B$. Typically, they decay to zero within a certain time scale, characterized by a bath correlation time τ_c, which depends on the particular bath parameters. In the next section, we explicitly consider the bath correlation functions relevant for our model applications.

2.3 Harmonic bath and its correlation functions

There exists a number of models developed to describe the bath and the system-bath coupling [37, 54]. In this work, we model the dissipative environment as a bath of independent harmonic oscillators,

$$H_B = \sum_q \frac{\omega_q}{2}(p_q^2 + q_q^2), \tag{23}$$

where q_q and p_q are dimensionless coordinate and momentum operators of the bath. For simplicity, we restrict ourselves to a single system-coordinate case, $\mathbf{Q} \equiv Q$, and assume a linear system-bath interaction

$$H_{SB} = Q\sum_q g_q q_q, \tag{24}$$

where g_q describe the system-bath coupling strength. The parameters of the bath are characterized by the bath spectral function

$$J(\omega) = \frac{\pi}{2}\sum_q g_q^2 \delta(\omega - \omega_q). \tag{25}$$

With the help of (20) it is straightforward to extract the bath operators from (24)

$$F = \sum_q g_q q_q, \tag{26}$$

and to obtain the following expression for the harmonic-bath correlation functions

$$\begin{aligned}\langle FF(\tau)\rangle_B &= \frac{1}{2}\sum_q g_q^2(e^{-i\omega_q\tau} + 2n(\omega_q)\cos\omega_q\tau),\\ \langle F(\tau)F\rangle_B = \langle FF(\tau)\rangle_B^* &= \frac{1}{2}\sum_q g_q^2(e^{i\omega_q\tau} + 2n(\omega_q)\cos\omega_q\tau).\end{aligned} \tag{27}$$

Here,

$$n(\omega) = 1/(e^{\omega/kT} - 1) \tag{28}$$

is the Bose distribution function. The summation over bath modes in (27) can be replaced by an integration, which yields[3]

$$\langle FF(\tau)\rangle_B = \int_0^\infty d\omega \frac{1}{\pi} J(\omega)(e^{-i\omega\tau} + 2n(\omega)\cos\omega\tau). \tag{29}$$

Let us consider the bath correlation functions explicitly for the case of the Ohmic spectral density [40]

$$J(\omega) = \eta\omega e^{-\omega/\omega_c}, \tag{30}$$

where η is a dimensionless parameter, characterizing the system-bath coupling strength, and ω_c is a bath cut-off frequency. We shall use the spectral function of this type in the ET-model calculations. Spectral densities of real chemical systems are, of course, more complicated, but the ohmic form (30) is believed to catch their principle features and is widely adopted in quantum theory of dissipative systems [37].

The integration over ω in the expression (29) can be done analytically for the two limiting cases of very low temperature, $kT \ll \omega_c$, and very high temperature, $kT \gg \omega_c$, when the distribution function in the integrand can be either approximated by zero or as

$$n(\omega) \simeq \frac{kT}{\omega}. \tag{31}$$

We adopt the form (31), having in mind that it is zero for the low-temperature regime. The integration over ω in (29) gives

$$\langle F_k F_k(\tau)\rangle_B = \frac{\eta}{\pi}\omega_c^2 C(\tau), \tag{32}$$

where

$$C(\tau) = \frac{2kT/\omega_c(1+\omega_c^2\tau^2) + (1-\omega_c^2\tau^2) - i2\omega_c\tau}{(1+\omega_c^2\tau^2)^2} \tag{33}$$

[3]For simplicity, we only consider $\langle FF(\tau)\rangle_B$.

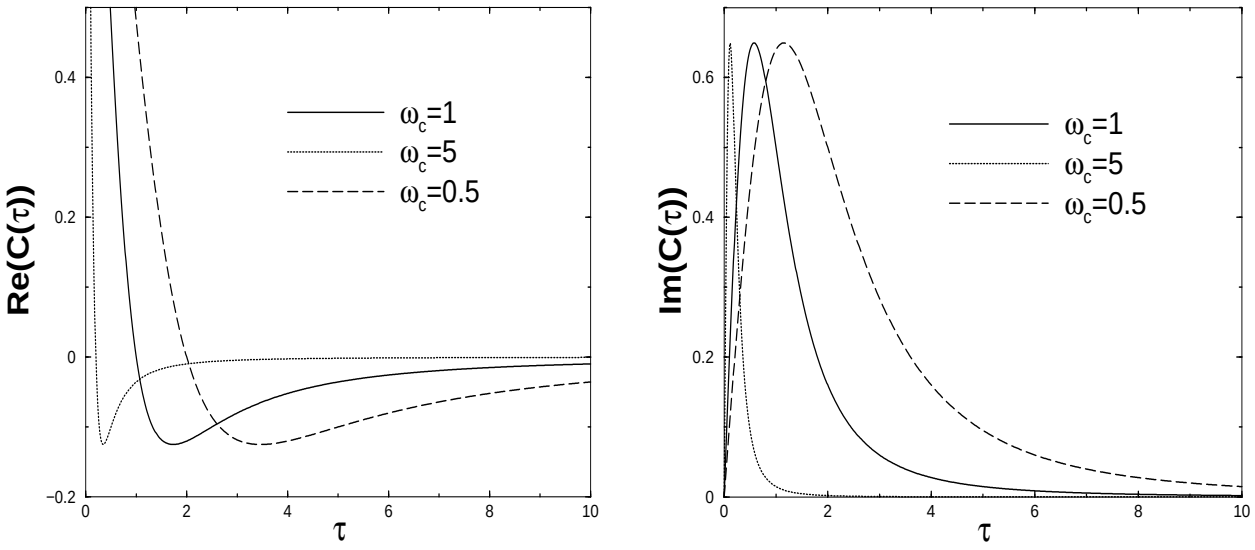

FIG. 1: Time-dependent components of the bath correlation functions (33) (real and imaginary parts) for different values of the cut-off frequency ω_c and zero temperature.

is the time-dependent part of the bath correlation functions. Fig. 1 displays $C(\tau)$ for different cut-off frequencies and zero temperature. They are seen to decay to zero at a time scale which is defined by the cut-off frequency ω_c: the larger ω_c, the faster is the decay of the bath correlation functions. As can be seen from (29), only the real parts of the bath correlation functions are influenced by the temperature. In the high-temperature limit, (33), they evolve in time approximately as

$$\frac{1}{(1+\omega_c^2\tau^2)},$$

that is, exhibit the same ω_c-dependence as for the zero-temperature case. The bath correlation time is thus proportional to $1/\omega_c$ and can be roughly estimated as $\tau_c \approx 10/\omega_c$ from Fig. 1.

2.4 Approximations to Redfield theory

Although Redfield theory itself is already approximative in its nature, there are several further assumptions which are usually introduced in order to simplify its implementation. The most popular simplifications are the so-called stationary Redfield-tensor approximation

and the secular approximation. A time-independent Redfield tensor is used in eq. (16) when the stationary Redfield-tensor approximation is implied. The secular approximation, on the other hand, allows to decouple the Redfield equation, (16), in two separate equations for diagonal and off-diagonal elements of the RDM, an analytical solution being obtained for the latter.

The stationary Redfield-tensor approximation is very often not distinguished from the Markov approximation, as it is supposed to be satisfied whenever the Markov approximation is valid. It appears, however, that the validity of the Markov approximation is a necessary, but not sufficient condition.

The application of the secular approximation is stimulated by the perturbative treatment of the system-bath coupling. The statement that the secular terms are affected by the perturbation much more than all the other ones is, of course, correct, but the usual definition of these terms is not strict enough, as will be discussed below.

2.4.1 Stationary Redfield tensor

The Redfield tensor elements are generally time-dependent and their time evolution is determined by the time integrals in (22), in particular, by the bath correlation functions. The assumption of the Markovian system dynamics (12) implies very short-living system-bath interactions and the bath correlation functions are thus supposed to decay to zero at a very short time scale. This consideration is the basis for the stationary Redfield-tensor approximation: the Redfield tensor is assumed to be time-independent for all t and its stationary value is calculated by replacing the upper integration limit in (22) by infinity ($t \to \infty$).

The decay of the bath correlation functions does result in the convergence of the time-dependent Redfield tensor to its stationary value, but the corresponding time scale (we denote it as τ_{st} for convenience) is finite, even if the Markov approximation is fulfilled, and also influenced by the frequencies of eigenstate pairs $\Omega = \{\omega_{\mu\kappa}, \omega_{\lambda\nu}\}$ in the exponents of

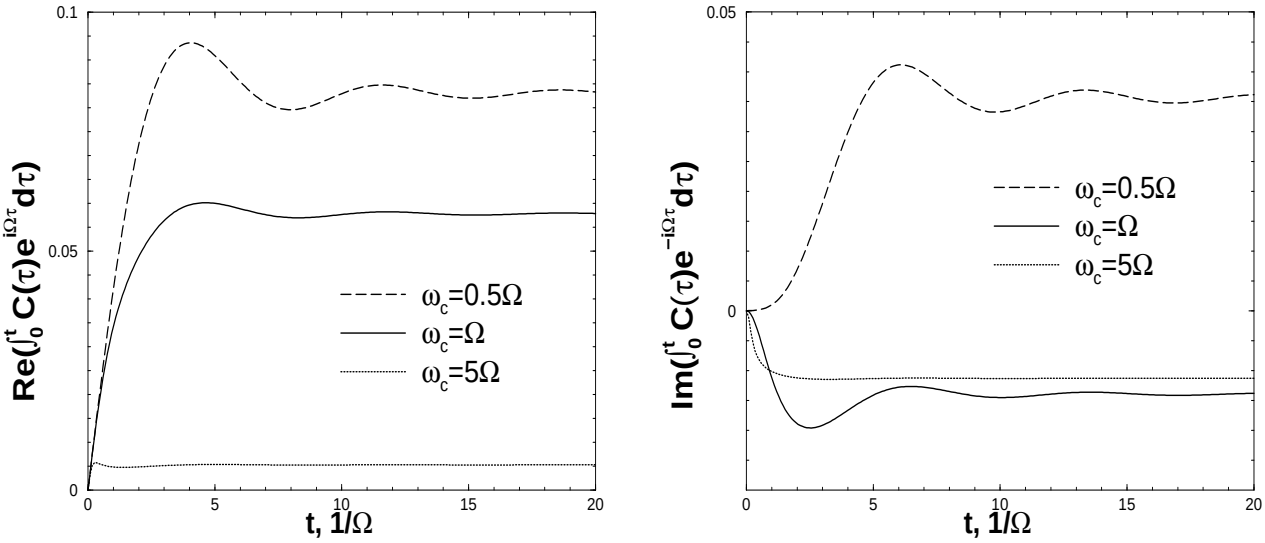

FIG. 2: The integrals $\int_0^t d\tau C(\tau)e^{-i\Omega\tau}$, where $C(\tau)$ is the time-dependent part of the harmonic-bath correlation functions (33), for a fixed Ω and different cut-off frequencies ω_c in the zero-temperature limit.

the time integrals in (22). Consequently, the initial system evolution, $0 < t < \tau_{st}$, cannot be properly described if the stationary Redfield-tensor approximation is involved, and the Redfield-tensor becomes constant only for $t > \tau_{st}$. Fig. 2 shows the convergence of real and imaginary parts of the integrals

$$\int_0^t d\tau C(\tau)e^{-i\Omega\tau},$$

where $C(\tau)$ is the time-dependent part of the harmonic-bath correlation functions (33), for a fixed Ω and different ω_c in the zero-temperature limit. It is seen that the increase of ω_c (that is, the decrease of the bath correlation time τ_c) does accelerate the convergence of the integrals towards the stationary value, but the time scale in Fig. 2 has $1/\Omega$ units and a slower in absolute units convergence is expected for smaller eigenfrequencies Ω.

The error introduced by the stationary approximation depends on the system and system-bath coupling parameters, but is normally rather small. The approximation can be thus very advantageous, as it simplifies considerably evaluation of the Redfield tensor elements: the integrals are to be calculated just once, but not at every time step. For the case of the

harmonic bath, the Redfield-tensor components (22) read

$$\Gamma^{+}_{\lambda\nu\mu\kappa} = \langle\lambda|Q|\nu\rangle\langle\mu|Q|\kappa\rangle \int_0^t d\tau \int_0^\infty d\omega \frac{1}{\pi} J(\omega)(e^{-i\omega\tau} + 2n(\omega)\cos\omega\tau)e^{-i\omega_{\mu\kappa}\tau},$$
$$\Gamma^{-}_{\lambda\nu\mu\kappa} = \langle\lambda|Q|\nu\rangle\langle\mu|Q|\kappa\rangle \int_0^t d\tau \int_0^\infty d\omega \frac{1}{\pi} J(\omega)(e^{i\omega\tau} + 2n(\omega)\cos\omega\tau)e^{-i\omega_{\lambda\nu}\tau}. \quad (34)$$

The replacement $t \to \infty$ in (34) allows a straightforward evaluation of the time integrals

$$\int_0^\infty d\tau \cos(\omega\tau)e^{-i\Omega\tau} = \frac{1}{2}\left(\int_0^\infty d\tau e^{-i(\omega+\Omega)\tau} + \int_0^\infty d\tau e^{i(\omega-\Omega)\tau}\right), \quad (35)$$

$$\int_0^\infty d\tau e^{\pm i(\omega\mp\Omega)\tau} = \pi\delta(\omega \mp \Omega) \pm i\mathcal{P}\frac{1}{\omega \mp \Omega} \quad (36)$$

(here $\mathcal{P}$ is the Cauchy principal part) and leads to the the analytical evaluation of the real part of the Redfield tensor

$$\mathrm{Re}(\Gamma^{+}_{\lambda\nu\mu\kappa}) = \langle\lambda|Q|\nu\rangle\langle\mu|Q|\kappa\rangle \begin{cases} J(\omega_{\kappa\mu})(1+n(\omega_{\kappa\mu})) & \text{if } \omega_\kappa > \omega_\mu \\ J(\omega_{\mu\kappa})n(\omega_{\mu\kappa}) & \text{if } \omega_\mu > \omega_\kappa \\ \lim_{\omega\to 0} J(\omega)n(\omega)^4 & \text{if } \omega_\mu = \omega_\kappa \end{cases}$$
$$\mathrm{Re}(\Gamma^{-}_{\lambda\nu\mu\kappa}) = \langle\lambda|Q|\nu\rangle\langle\mu|Q|\kappa\rangle \begin{cases} J(\omega_{\lambda\nu})(1+n(\omega_{\lambda\nu})) & \text{if } \omega_\lambda > \omega_\nu \\ J(\omega_{\nu\lambda})n(\omega_{\nu\lambda}) & \text{if } \omega_\nu > \omega_\lambda \\ \lim_{\omega\to 0} J(\omega)n(\omega) & \text{if } \omega_\nu = \omega_\lambda \end{cases}, \quad (37)$$

while for the imaginary part (so-called Lamb shift) the principal-value integrals need to be calculated

$$\mathrm{Im}(\Gamma^{+}_{\lambda\nu\mu\kappa}) = \langle\lambda|Q|\nu\rangle\langle\mu|Q|\kappa\rangle \left(\mathcal{P}\int_0^\infty d\omega \frac{J(\omega)n(\omega)}{\omega - \omega_{\mu\kappa}} - \mathcal{P}\int_0^\infty d\omega \frac{J(\omega)(1+n(\omega))}{\omega - \omega_{\kappa\mu}}\right)$$
$$\mathrm{Im}(\Gamma^{-}_{\lambda\nu\mu\kappa}) = \langle\lambda|Q|\nu\rangle\langle\mu|Q|\kappa\rangle \left(\mathcal{P}\int_0^\infty d\omega \frac{J(\omega)(1+n(\omega))}{\omega - \omega_{\lambda\nu}} - \mathcal{P}\int_0^\infty d\omega \frac{J(\omega)n(\omega)}{\omega - \omega_{\nu\lambda}}\right). \quad (38)$$

2.4.2 Secular approximation

Being a consequence of the perturbative treatment of the system-bath coupling, the secular approximation has been already proposed by Redfield [49] and widely accepted in

[4]For the Ohmic spectral density (30) we have $\lim_{\omega\to 0} J(\omega)n(\omega) = \eta kT$.

further developments of Redfield theory for relaxational processes [38, 39, 74]. In analogy to the perturbation theory of the Schrödinger equation, it can be argued that the effect of so-called secular terms of the Redfield tensor in equation (16), which connect states that are very close or degenerate in the eigenfrequencies $\Omega = \{\omega_{\mu\nu}, \omega_{\kappa\lambda}\}$, is much more pronounced than that of all the other ones, which satisfy

$$|R_{\mu\nu\kappa\lambda}| \ll |\omega_{\mu\nu} - \omega_{\kappa\lambda}| \tag{39}$$

and thus allow a perturbative treatment. However, in most applications of the secular approximation [38, 39, 74], only couplings with strictly degenerate eigenfrequencies

$$|\omega_{\mu\nu} - \omega_{\kappa\lambda}| = 0 \tag{40}$$

are taken into account. The secular approximation is usually rationalized using the interaction representation of the RDM

$$\sigma^I_{\mu\nu}(t) = e^{iH_s t}\sigma_{\mu\nu}(t)e^{-iH_s t}, \tag{41}$$

and Redfield equation in the interaction picture

$$\frac{\partial\sigma^I_{\mu\nu}(t)}{\partial t} = \sum_{\kappa\lambda} R_{\mu\nu\kappa\lambda}\sigma^I_{\kappa\lambda}(t)e^{i(\omega_{\mu\nu}-\omega_{\kappa\lambda})t}. \tag{42}$$

When both sides in eq. (42) are integrated over a time interval Δt and (i) the RDM does not change considerably during Δt and (ii) $\Delta t \gg (\omega_{\mu\nu} - \omega_{\kappa\lambda})^{-1}$, then the integral averages to zero, because of the fast oscillating exponential terms. This does not happen, however, for the secular terms, i.e., when $\omega_{\mu\nu} = \omega_{\kappa\lambda}$.

It is widely ignored that if the difference $\omega_{\mu\nu} - \omega_{\kappa\lambda}$ is smaller than or of the order of magnitude of the corresponding Redfield-tensor element

$$|\omega_{\mu\nu} - \omega_{\kappa\lambda}| \lesssim |R_{\mu\nu\kappa\lambda}|, \tag{43}$$

conditions (i) and (ii) are not fulfilled simultaneously and the corresponding terms are of the same importance as the secular terms, for which eq. (40) is strictly satisfied. Their neglect in

the propagation of the RDM leads to an inaccurate description of the relaxational dynamics. The effect of their exclusion becomes more pronounced when the system-bath coupling strength increases and/or many energy levels are involved in the relaxational dynamics and possibly coupled by the "non-strictly" secular, (43), elements of the Redfield tensor.

On the other hand, if the eigenlevel structure is not dense and the non-strictly secular terms, (43), are not present, the usual secular approximation, based on eq. (40), is very favorable. If the system eigenstates are not degenerate, it leads to a decoupling of eq. (16) in two separate equations for diagonal and off-diagonal terms of the RDM, that is for populations and coherences. The diagonal terms obey the Pauli master equation

$$\frac{\partial \sigma_{\mu\mu}(t)}{\partial t} = \sum_{\nu \neq \mu} \gamma_{\mu\nu} \sigma_{\nu\nu}(t) - \Gamma_{\mu\mu} \sigma_{\mu\mu}(t), \tag{44}$$

while for the off-diagonal terms, for the case of unequally spaced system energy levels, an analytical solution is obtained

$$\sigma_{\mu\nu}(t) = \sigma_{\mu\nu}(0) e^{-i\omega_{\mu\nu}t} e^{-\Gamma_{\mu\nu}t}. \tag{45}$$

The relaxation rates $\gamma_{\mu\nu}$ and $\Gamma_{\mu\nu}$ correspond to the secular elements of the Redfield tensor

$$\gamma_{\mu\nu} = R_{\mu\mu\nu\nu} \text{ for all } \mu \neq \nu; \quad \Gamma_{\mu\nu} = -R_{\mu\nu\mu\nu}. \tag{46}$$

The Pauli master equation for the populations (44) can be easily interpreted: $\gamma_{\mu\nu}$ are real and represent a loss of the population from a state μ to a state ν. On the other hand, it can be shown that

$$\Gamma_{\mu\mu} = -\sum_{\alpha \neq \mu} \gamma_{\alpha\mu},$$

so that the last term in (44) describes the gain in the population to the energy level μ from all the other levels.

Off-diagonal rates $\Gamma_{\mu\nu}$, which enter eq. (45) for the coherences, are complex. Their real parts can be expressed as

$$Re(\Gamma_{\mu\nu}) = -\frac{1}{2}(\Gamma_{\mu\mu} + \Gamma_{\nu\nu}) - \Gamma^{ph}_{\mu\nu},$$

where

$$\Gamma^{ph}_{\mu\nu} = \Gamma^{+}_{\nu\nu\mu\mu} + \Gamma^{-}_{\nu\nu\mu\mu}$$

causes no transition between different eigenstates, but a phase change. It vanishes if the diagonal elements of the system operators in the system-eigenstate representation are zero. The imaginary part of $\Gamma_{\mu\nu}$ represents the Lamb shift

$$Im(\Gamma_{\mu\nu}) = \sum_{\alpha} Im(\Gamma^{+}_{\mu\alpha\alpha\mu}) + Im(\Gamma^{-}_{\nu\alpha\alpha\nu}).$$

From the computational point of view, the secular approximation is very attractive, as numerical time propagation is required only for the diagonal terms.

2.5 Limitations of Redfield theory

The principal and unavoidable limitation of the Redfield-theory description is its perturbative character. It is not straightforward, however, to define a parameter, which has to be small. The stationary limit of the real part of the Redfield-tensor elements is proportional to $J(\Omega)(1 + n(\Omega))$ and the requirement for the perturbative treatment to be successful can be formulated as

$$\frac{J(\Omega)(1 + n(\Omega))}{\Omega} \ll 1. \tag{47}$$

For the ohmic spectral density (30), the condition (47) leads to the following requirement for the system-bath coupling parameter η

$$\eta \ll e^{\Omega/\omega_c}(1 - e^{-\Omega/kT}). \tag{48}$$

The expression on the rhs of (48) is rather difficult to estimate as it depends not only on the bath cut-off frequency ω_c and temperature, but also on the particular system eigenfrequencies Ω. However, it is seen to be minimal in the range of the small eigenfrequencies $\Omega \ll \omega_c$, $\Omega \ll kT$. It means, that the couplings between very close (quasi-degenerate) eigenlevels (the presence of such levels is a common feature in the ET-modeling, especially when several

reactive modes are included in the system Hamiltonian and the eigenstate spectrum is very dense) are the strongest possible for given system-bath coupling parameters. On the other hand, the couplings between eigenlevels which are far from each other in the energy are negligible.

In the limit of zero temperature the situation simplifies and the requirement (48) reduces to

$$\eta \ll e^{\Omega/\omega_c},$$

a sufficient condition of which is given by

$$\eta \ll 1. \tag{49}$$

Unfortunately, no analogous expression can be obtained for the finite-temperature regime. Although, it can be noticed from the inequality (48), that smaller values of η, compared to the zero-temperature case, are required to provide the same accuracy of the perturbative treatment. Thus the inclusion of temperature can limit the applicability of Redfield theory.

The assumption of Markovian system dynamics (12) is believed to be another critical point in the Redfield-theory description. However, as was mention in section 2.2, it must be satisfied if the perturbation treatment of the system-bath coupling is valid.

3. MODELING OF ULTRAFAST ELECTRON TRANSFER: THEORETICAL CONCEPTS

The basic theoretical models for the interpretation of ET phenomena are the Marcus theory [4] and the Golden Rule (GR) formula [6] for nonadiabatic electron transfer. According to the Marcus expression, the ET rate is determined by such macroscopic parameters as free energy and temperature. In the Golden-Rule formulation, the electronic inter-state coupling is assumed to be the rate-determining factor, and the irreversibility of the transfer is ensured by solvent relaxation.

In recent years, the attention has shifted towards ET processes in the femtosecond regime, so-called ultrafast ET processes. ET time scales in the 10-100 fs regime have been observed in a variety of organic donor-acceptor complexes and mixed-valence compounds [10, 16–19, 30, 31], as well as in biological systems, in particular in the photosynthetic reaction centers [26].

Occurring faster than vibrational relaxation takes place, ultrafast ET reactions often exhibit vibrational wave-packet motion in electronic donor and/or acceptor states [18, 19, 25, 27–29, 31, 32]. In these experiments, the donor state is usually prepared by a quasi-instantaneous excitation with an ultrashort (10-20 fs) laser pulse. A moving wave-packet can be thus formed in this state due to different equilibrium nuclear geometries in electronic ground and excited states. Wave-packet motion in the product state (or in the ground state in the case of a back-ET reaction) can be caused by the nonadiabatic electronic interaction with the donor state, that is by the ET itself.

To account for the effect of fast and underdamped intramolecular modes, Barabara and collaborators [13] have extended the standard Golden Rule rate formula to include a high-frequency quantum mode, combining the developments of Sumi and Marcus [9] and of Jortner and Bixon [8]. The effects of the nonequilibrium initial state have been addressed in Refs. [35, 75, 76]. The drawback of these formulations is a perturbative treatment of the ET coupling, which can be questioned for ET processes in the femtosecond regime.

Redfield theory, which has been applied by several groups to a variety of quantum systems in a dissipative environment [48, 57, 58, 77, 61, 78–83], allows to overcome the limitations of the GR approach and is very well suited for the investigation of the interplay of strong electronic coupling, coherent vibrational motion in high-frequency quantum modes and dissipation by the thermal environment. The energetically accessible electronic states and one or few strongly coupled reaction modes constitute the system, while the remaining intramolecular and solvent degrees of freedom represent the bath in the system-bath partitioning required by the RDM formalism.

3.1 Model Hamiltonian

Adopting the system-bath approach, we express the model Hamiltonian as a sum of system and bath Hamiltonians and a system - bath interaction operator (6). In the present context, the electronic states and vibrational modes which are directly involved in the reaction constitute the relevant system and are described by the system Hamiltonian H_S. The bath degrees of freedom are only indirectly involved via the system-bath coupling H_{SB}, which is assumed to be weaker than the primary interactions contained in the system Hamiltonian.

In the diabatic representation [84–87] of the electronic states, corresponding to different locations of the electron, the model Hamiltonian of the system is written as

$$H_S = \sum_{i}^{N_e} |\phi_i\rangle(h_i + \varepsilon_i)\langle\phi_i| + \sum_{i\neq j}^{N_e} |\phi_i\rangle V_{ij}\langle\phi_j|. \tag{50}$$

Here, N_e is the number of the diabatic electronic states, $|\phi_i\rangle$, involved in the reaction, V_{ij} are electronic coupling matrix elements, ε_i are vertical electronic excitation energies and h_i denote the vibrational Hamiltonian, pertaining to the electronic state $|\phi_i\rangle$. We assume the electronic couplings V_{ij} to be constant (independent of the vibrational coordinates) and restrict ourselves to a single system-mode case. The harmonic approximation for the vibrational motion is implied[5] and the system reaction mode is assumed to be linearly

[5]For the study of anharmonic effects see, e.g., Ref. [88].

coupled to the bath of harmonic oscillators (23), (24).

The system vibrational Hamiltonians are thus written as

$$h_i = \frac{\omega_0}{2}(P^2 + Q^2) + \kappa^{(i)}Q + Q^2 \sum_q \frac{g_q^2}{2\omega_q}, \tag{51}$$

where Q denotes the dimensionless reaction coordinate and $P = -i\frac{\partial}{\partial Q}$ is the corresponding momentum operator. The vibrational frequency of the reaction mode ω_0 is assumed to be the same for both electronic states. The parameters $\kappa^{(i)}$ describe the electronic - vibrational coupling.

The diabatic potential functions for the system mode are thus shifted parabolas. In the absence of dissipation, their horizontal displacements from the energy minimum of the electronic ground state are determined as

$$\Delta^{(i)} = -\kappa^{(i)}/\omega_0,$$

and the vertical displacements are given by

$$\varepsilon_{\mathrm{ad}}^{(i)} = \varepsilon_i - (\kappa^{(i)})^2/2\omega_0.$$

The last term in (51) is a so-called renormalization term, which renormalizes the system PE surfaces when the system-bath coupling is not zero. For a given spectral function the renormalizing factor $\sum_q \frac{g_q^2}{2\omega_q}$ is explicitly evaluated as

$$\sum_q \frac{g_q^2}{2\omega_q} = \int_0^\infty d\omega \frac{J(\omega)}{\pi\omega}. \tag{52}$$

For the Ohmic spectral density (30), in particular, one obtains

$$\sum_q \frac{g_q^2}{2\omega_q} = \frac{\eta\omega_c}{\pi}. \tag{53}$$

The renormalization of the system PE surfaces is usually neglected, if the imaginary part of the relaxation operator (Redfield tensor) is not taken into account.

3.2 Rotating-wave approximation

The rotating-wave approximation (RWA) for the linear system-bath coupling operator has been introduced for a damped harmonic oscillator [38] and later adopted for the ET modeling [52, 59, 61], within the harmonic approximation for vibrational motion. The system-bath interaction operator (24) can then be written in the second quantization representation

$$H_{SB} = \sum_q \frac{g_q}{2}(b^\dagger + b)(a_q^\dagger + a_q), \tag{54}$$

where b, $b^\dagger$ and a_q, $a_q^\dagger$ are the annihilation and creation operators for the system and bath modes respectively. In the RWA, the system-bath coupling is approximated as

$$H_{SB}^{RWA} = \sum_q \frac{g_q}{2}(b^\dagger a_q + b a_q^\dagger), \tag{55}$$

i.e., the terms ba_q and $b^\dagger a_q^\dagger$ are neglected. While describing the dynamics of a damped harmonic oscillator with a frequency ω, it is argued that $e^{\pm i(\omega+\omega_q)t}$ terms, which arise from ba_q and $b^\dagger a_q^\dagger$ components, can be neglected compared to $e^{\pm i(\omega-\omega_q)t}$ terms, resulting from $b^\dagger a_q$ and $ba_q^\dagger$ multiplication, for $\omega \simeq \omega_q$ and times of interest[6]. The RWA system-bath interaction operator can be also written in the factorized form (20) with system operators

$$Q_1 = b, \quad Q_2 = b^\dagger, \tag{56}$$

and bath operators

$$F_1 = \sum_q \frac{g_q}{2} a_q^\dagger, \quad F_2 = \sum_q \frac{g_q}{2} a_q. \tag{57}$$

[6]For the discussion of the RWA for a damped harmonic oscillator see, e.g., Ref. [89].

If the RWA is invoked for H_{SB} in the Redfield-theory formalism, the stationary values of the Redfield-tensor components (37), (38) can be expressed as

$$\mathrm{Re}(\Gamma^{+}_{\lambda\nu\mu\kappa}) = \begin{cases} \frac{1}{2}\langle\lambda|b^{\dagger}|\nu\rangle\langle\mu|b|\kappa\rangle J(\omega_{\kappa\mu})(1+n(\omega_{\kappa\mu})) & \text{if } \omega_{\kappa} > \omega_{\mu} \\ \frac{1}{2}\langle\lambda|b|\nu\rangle\langle\mu|b^{\dagger}|\kappa\rangle J(\omega_{\mu\kappa})n(\omega_{\mu\kappa}) & \text{if } \omega_{\mu} > \omega_{\kappa} \\ \frac{1}{2}(\langle\lambda|b^{\dagger}|\nu\rangle\langle\mu|b|\mu\rangle + \langle\lambda|b|\nu\rangle\langle\mu|b^{\dagger}|\mu\rangle)\lim_{\omega\to 0} J(\omega)n(\omega) & \text{if } \omega_{\mu} = \omega_{\kappa}, \end{cases}$$

$$\mathrm{Re}(\Gamma^{-}_{\lambda\nu\mu\kappa}) = \begin{cases} \frac{1}{2}\langle\lambda|b^{\dagger}|\nu\rangle\langle\mu|b|\kappa\rangle J(\omega_{\lambda\nu})(1+n(\omega_{\lambda\nu})) & \text{if } \omega_{\lambda} > \omega_{\nu} \\ \frac{1}{2}\langle\lambda|b|\nu\rangle\langle\mu|b^{\dagger}|\kappa\rangle J(\omega_{\nu\lambda})n(\omega_{\nu\lambda}) & \text{if } \omega_{\nu} > \omega_{\lambda} \\ \frac{1}{2}(\langle\nu|b^{\dagger}|\nu\rangle\langle\mu|b|\kappa\rangle + \langle\nu|b|\nu\rangle\langle\mu|b^{\dagger}|\kappa\rangle)\lim_{\omega\to 0} J(\omega)n(\omega) & \text{if } \omega_{\nu} = \omega_{\lambda}, \end{cases} \tag{58}$$

$$\begin{aligned} \mathrm{Im}(\Gamma^{+}_{\lambda\nu\mu\kappa}) =& \tfrac{1}{2}\langle\lambda|b|\nu\rangle\langle\mu|b^{\dagger}|\kappa\rangle\mathcal{P}\int_0^{\infty} d\omega \frac{J(\omega)n(\omega)}{\omega-\omega_{\mu\kappa}} \\ & -\tfrac{1}{2}\langle\lambda|b^{\dagger}|\nu\rangle\langle\mu|b|\kappa\rangle\mathcal{P}\int_0^{\infty} d\omega \frac{J(\omega)(1+n(\omega))}{\omega-\omega_{\kappa\mu}}, \\ \mathrm{Im}(\Gamma^{-}_{\lambda\nu\mu\kappa}) =& \tfrac{1}{2}\langle\lambda|b^{\dagger}|\nu\rangle\langle\mu|b|\kappa\rangle\mathcal{P}\int_0^{\infty} d\omega \frac{J(\omega)(1+n(\omega))}{\omega-\omega_{\lambda\nu}} \\ & -\tfrac{1}{2}\langle\lambda|b|\nu\rangle\langle\mu|b^{\dagger}|\kappa\rangle\mathcal{P}\int_0^{\infty} d\omega \frac{J(\omega)n(\omega)}{\omega-\omega_{\nu\lambda}}. \end{aligned} \tag{59}$$

3.3 Diabatic damping model

The diabatic-damping model (DDM) for the description of the dynamics of electronically coupled dissipative systems has been often employed for the ultrafast-ET modeling [50, 52, 59, 60]. It is similar to Redfield theory as the relaxation is described perturbatively, but it neglects the electronic coupling as far as the dissipation is concerned (the relaxation operator, derived by Takagahara *et al.* [46] for a damped harmonic mode in a system of uncoupled electronic states, is adopted). As a result, a rather simple relaxation operator of Lindblad form is obtained for the case of harmonic diabatic potentials, the RWA being assumed for the system-bath coupling.

The DDM relaxation operator can be also derived from the Redfield operator (21). In contrast to the traditional Redfield approach, this is not the system reaction coordinate Q,

but the coordinates of the displaced harmonic oscillators

$$Q^{(i)} = Q - \Delta^{(i)},$$

which are coupled to the harmonic bath. The corresponding system-bath interaction operator in the RWA reads

$$\tilde{H}_{SB} = \sum_{iq} |\phi_i\rangle \frac{g_q}{2} (b^{(i)\dagger} a_q + b^{(i)} a_q^\dagger) \langle\phi_i| \tag{60}$$

where $b^{(i)}$ and $b^{(i)\dagger}$ are the annihilation and creation operators of the displaced oscillators and can be expressed as

$$b^{(i)} = b - \Delta^{(i)}/\sqrt{2},$$

$$b^{(i)\dagger} = b^\dagger - \Delta^{(i)}/\sqrt{2}.$$

The operator (60) can be also represented in the factorized form (20) with system operators

$$\tilde{Q}_1 = \sum_i^{Ne} |\phi_i\rangle b^{(i)} \langle\phi_i|, \quad \tilde{Q}_2 = \sum_i^{Ne} |\phi_i\rangle b^{(i)\dagger} \langle\phi_i| \tag{61}$$

and bath operators (57). The DDM relaxation operator is then obtained from (21) with system and bath operators (61), (57) by extending the upper integration limit to infinity (cf. section 2.4.1) and approximating H_S by

$$\tilde{H}_S = \sum_i |\phi_i\rangle H_i \langle\phi_i|,$$

while calculating $\tilde{Q}_k(\tau)$. The resulting expression is in closed form and allows the eigenstate-free propagation of the reduced density matrix

$$R_{DDM}(\sigma) = \sum_{ij}^{N_e} \frac{\Gamma}{2} |\phi_i\rangle \lambda^{(ij)} \langle\phi_j|, \tag{62}$$

where

$$\lambda_k^{(ij)} = (n(\omega_0) + 1)(2b^{(i)}\sigma^{(ij)}b^{(j)\dagger} - b^{(i)\dagger}b^{(i)}\sigma^{(ij)} - \sigma^{(ij)}b^{(j)\dagger}b^{(j)})$$

$$+ n(\omega_0)(2b^{(i)\dagger}\sigma^{(ij)}b^{(j)} - b^{(i)}b^{(i)\dagger}\sigma^{(ij)} - \sigma^{(ij)}b^{(j)}b^{(j)\dagger}).$$

Here, $\sigma^{(ij)} = \langle\phi_i|\sigma|\phi_j\rangle$ are matrix elements of RDM in the diabatic electronic representation, and Γ is a damping parameter, given by the value of the spectral function at the system-mode frequency, $\Gamma = J(\omega_0)$.

Since the diagonalization of the system Hamiltonian is not required in the DDM, the calculations are not necessarily limited to systems with few reaction modes (which is the case in the standard Redfield theory). Another advantage is that the relaxation operator is of Lindblad form. Therefore the Monte-Carlo wave function propagation scheme [56] can be easily implemented as an efficient computational tool [51]. It is convenient to obtain the RDM in the diabatic electronic representation, as the diabatic-state populations correspond to its diagonal elements. The matrix representation of the relaxation operator is structurally very sparse, which also reduces the numerical effort of the RDM propagation. The drawback of the DDM is that the asymptotic limit ($t \to \infty$) is not strictly correct, but it can nevertheless be very useful for short-time problems with weak to moderate electronic interaction.

3.4 Golden Rule

As any chemical reaction, ET is traditionally described in terms of a reaction rate. The traditional microscopic ET rate expression [6] is obtained adopting Fermi's Golden-Rule formula, which is well-known from the theory of radiative and radiationless transitions. The Golden-Rule (GR) formula is the result of perturbation theory with respect to the coupling which is responsible for the transition, and the transition rate from an initial state i to a final state f is found to be proportional to the square of the coupling matrix element between these states. Correspondingly, the GR ET rate is proportional to the square of the electronic coupling between the donor and acceptor state, $k_{ET} \sim |V_{\mathrm{DA}}|^2$. The rate description assumes exponential decay of the donor state population due to the electron transfer, i.e.

$$P_{\mathrm{D}}(t) = \exp(-k_{ET}t). \tag{63}$$

There is a variety of GR ET rate expressions [90, 91], which differ in technical details of the derivation. In order to compare GR predictions with RDM propagation results, the system, bath and system-bath interaction parameters should enter explicitly the GR expression for the ET rate. We propose the following procedure. First, the model reaction-mode Hamiltonian (6), (50), (23), (24) is unitary transformed to the normal-mode representation

$$H = \sum_{i}^{N_e} |\phi_i\rangle(\tilde{h}_i + \varepsilon_i)\langle\phi_i| + \sum_{i\neq j}^{N_e} |\phi_i\rangle V_{ij}\langle\phi_j| \tag{64}$$

with

$$\tilde{h}_i = \sum_{\alpha} \frac{\tilde{\omega}_\alpha}{2}(\tilde{p}_\alpha^2 + \tilde{q}_\alpha^2) + \tilde{\kappa}_\alpha^{(i)}\tilde{q}_\alpha. \tag{65}$$

Second, the GR ET rate expression in the steepest-descent approximation obtained in Ref. [92] (which is equivalent to that, derived from the Spin-Boson Hamiltonian [93]) is used for the Hamiltonian (64), (65).

The saddle-point expression for the ET rate thus reads

$$k_{ET} = V_{\rm DA}^2 \sqrt{\frac{2\pi}{|f''(t_s)|}} e^{f(t_s)}, \tag{66}$$

where

$$f(t) = i(\varepsilon_{ad}^{(\rm D)} - \varepsilon_{ad}^{(\rm A)})t - \sum_{\alpha} S_\alpha(2n(\tilde{\omega}_\alpha) + 1 - (n(\tilde{\omega}_\alpha) + 1)e^{-i\tilde{\omega}_\alpha t} - n(\tilde{\omega}_\alpha)e^{i\tilde{\omega}_\alpha t}),$$

and

$$\varepsilon_{ad}^{(i)} = \varepsilon_i - \sum_{\alpha} (\tilde{\kappa}_\alpha^{(i)})^2/2\tilde{\omega}_\alpha, \quad i = {\rm D}, {\rm A}; \quad S_\alpha = \frac{(\tilde{\kappa}_\alpha^{(\rm D)} - \tilde{\kappa}_\alpha^{(\rm A)})^2}{2\tilde{\omega}_\alpha^2}.$$

Here, $n(\omega)$ is the distribution function (28) an t_s is the saddle-point time chosen to satisfy $f'(t_s) = 0$.

4. MULTI-LEVEL REDFIELD THEORY FOR ULTRAFAST ELECTRON TRANSFER

Ultrafast excited-state electron transfer in the normal and inverted regions[7] is modeled by means of multi-level Redfield theory. A single harmonic reaction mode and two (sections 4.1, 4.2) or three (section 4.5) diabatic electronic states represent the system, while all other intramolecular and solvent degrees of freedom are considered as a dissipative environment and modeled as a bath of harmonic oscillators.

The reduced density matrix $\sigma(t)$ is numerically propagated in time according to eq. (16) by means a fourth-order Runge-Kutta algorithm, adopted from Ref. [94] (for the details of the numerical aspects see Appendix B). The stationary Redfield-tensor approximation and neglect of the Lamb shift (imaginary part of the Redfield tensor) are assumed in description of dissipation, and the system-bath coupling operator is defined in the RWA (55). Hence, the renormalization term is not included in the system Hamiltonian, and the Redfield-tensor components are given by (58).

Given $\sigma(t)$, the time-dependent expectation value of any system variable can be determined. The population probability of the initially prepared diabatic electronic state

$$P_i(t) = \mathrm{tr}\{\sigma(t)|\phi_i\rangle\langle\phi_i|\} \tag{67}$$

has been chosen as a representative observable to illustrate the ET process. In the three electronic-state models the population probability of every diabatic electronic state is monitored. Coherent wave-packet motion in the excited as well as in the ground electronic state is represented by a projection of the coordinate representation of the RDM (see Appendix A) to the corresponding electronic state.

Instantaneous excitation from the ground electronic state is assumed, i.e., at $t = 0$ a wave-packet is prepared in the donor state at equilibrium nuclear geometry of the ground electronic state. The initial conditions are referred to as stationary, if there is no shift

[7] For a classification of ET regions, see Appendix C.

between equilibrium configuration of the ground and excited electronic states (no moving wave packet prepared), and as nonstationary otherwise.

In the results reported below, we focus on ET reactions exhibiting vibrational wave-packet motion. We also discuss the validity range of the Golden-Rule approach and the performance of the secular and rotating-wave approximations, as well as the diabatic-damping model for the considered two electronic-state model examples.

4.1 Golden-Rule predictions vs. Redfield-theory simulations

Being non-perturbative in the electronic coupling, Redfield theory allows us to go beyond the GR approach and to explore the ranges of validity of the GR formula. We restrict ourselves here to a two electronic-state model with moderate bias, representing ET in the normal region. The system parameters are chosen as $\omega_0 = 0.05$eV, $\Delta^{(\mathrm{D})} = 2$, $\Delta^{(\mathrm{A})} = 5.5$, $\varepsilon_{ad}^{(\mathrm{D})} - \varepsilon_{ad}^{(\mathrm{A})} = 0.045$eV. The electronic coupling V_{DA} has been varied from $\omega_0/20 = 0.0025$eV to $\omega_0 = 0.05$eV. The donor (D) and acceptor (A) diabatic potential-energy (PE) curves with the zero-order vibrational levels are shown in the PE graph in Fig. 3 (full lines). The dotted lines in the PE graph indicate the adiabatic potential-energy functions for strong ($V_{\mathrm{DA}} = \omega_0$) and intermediate ($V_{\mathrm{DA}} = \omega_0/5$) values of the electronic coupling. The coupling of the system mode to the bath is described by the spectral function (30) with $\omega_c = \omega_0$ and the damping strength η is considered as a variable parameter.

The temperature is taken as zero to emphasize quantum tunneling effects. It is assumed that the system is prepared in the ground vibrational state of the donor diabatic potential at $t = 0$ (stationary initial conditions), that is there is no moving wave packet prepared and ET occurs in the relaxed system. The GR formula is thus expected to be applicable for small values of the electronic coupling.

The observable of interest is the population of the initially prepared diabatic well, i.e. $P_{\mathrm{D}}(t)$. The Redfield-theory results are obtained by the propagation of the RDM as defined in eq. (67), the Golden-Rule population probability is calculated by exponentiation of the

GR rate, eqs. (63), (66).

The results are shown in Fig. 3 on a ps time scale. In the first set of calculations we have assumed weak damping, $\eta = 0.1$ (Fig. 3a).

It is seen that the population dynamics, predicted by Redfield theory (solid lines) evolves with increasing $V_{\rm DA}$ from slow (ps) monotonous decay for small $V_{\rm DA}$ towards fast (fs) decay with pronounced quantum beats, which are damped on a ps time scale. The beatings reflect coherent electronic motion, analogous to the well-known Rabi oscillations in optical physics [95]. The frequency of these quantum beats is determined by the electronic coupling matrix element, renormalized by the Frank-Condon overlap integral of vibrational wave functions of the diabatic potentials. It increases therefore with increasing $V_{\rm DA}$. The fast oscillations becoming apparent for the largest $V_{\rm DA}$ arise from the fact that the initially prepared state deviates in this case from the eigenstates of the (significantly distorted) lower adiabatic potential.

The GR formula (dashed curves) provides, as expected, a reasonably accurate description of the ET dynamics in the regime $V_{\rm DA}/\omega_0 \leq \eta$, when the damping of the system mode is faster than the electronic inter-state dynamics, i.e., when $V_{\rm DA}$ is the rate-determining quantity. As $V_{\rm DA}$ increases, the relaxation dynamics in the final diabatic state can no longer compete with the electronic dynamics and electronic back-transfer becomes important [96]. Eventually, for $V_{\rm DA}/\omega_0 \gg \eta$, the population decay is controlled by the vibrational damping rate. As shown by Fig. 3a, the GR formula is able to describe the initial decay in this limit, but severely fails at longer times owing to the neglect of back-transfer[8].

This interpretation of the ET dynamics is confirmed by Fig. 3b, which gives the corresponding results for a stronger damping of the system mode, $\eta = 0.2$. The Rabi-type electronic oscillations are suppressed and the validity of the GR formula extends to larger values of $V_{\rm DA}$.

[8]Similar trends have been observed in the GR-validity test within path-integral calculations [97].

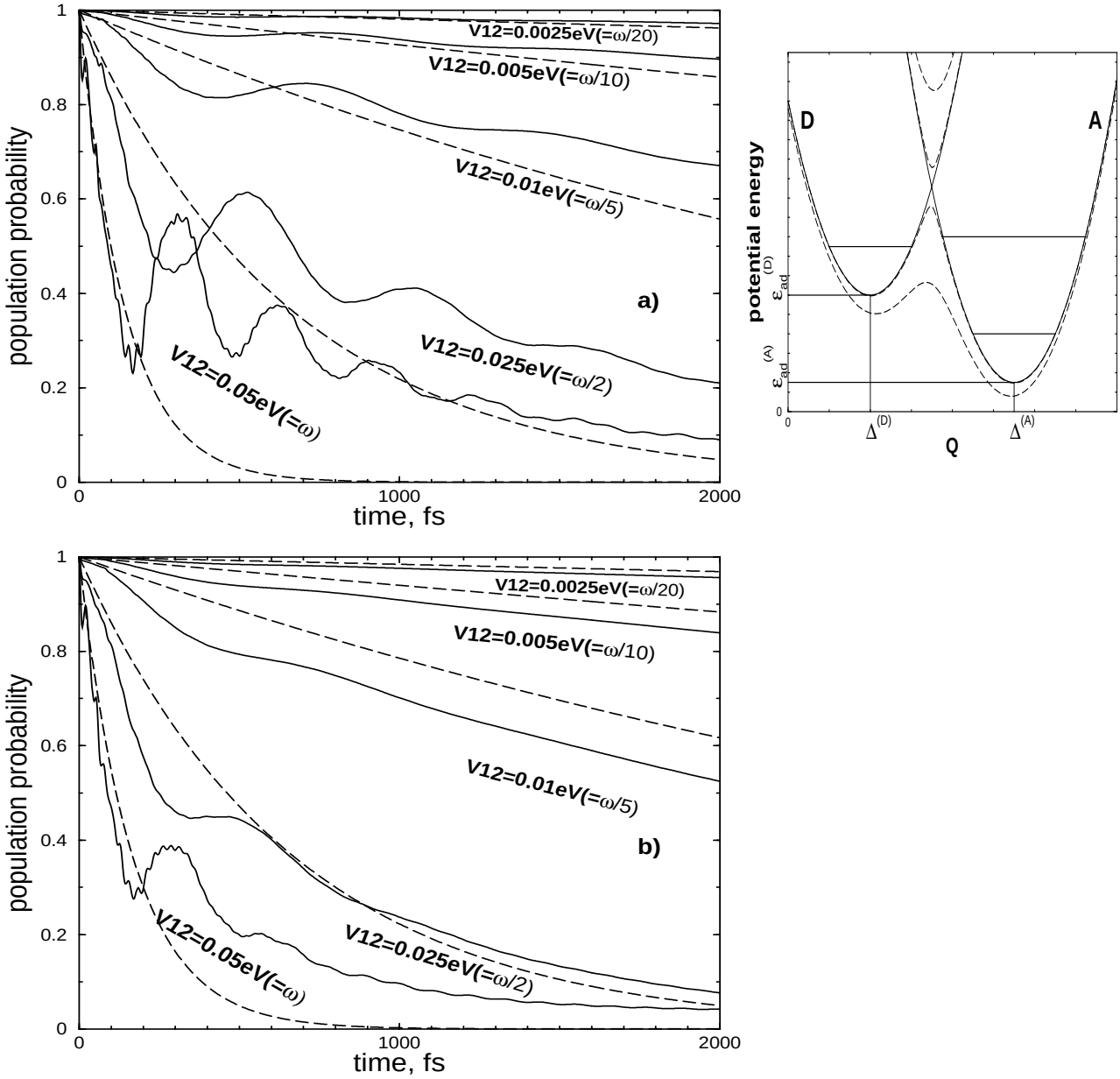

FIG. 3: Test of the validity of the Golden-Rule formula for ET in the normal region with stationary preparation. The time-dependent population probability $P_D(t)$ of the initially prepared diabatic electronic state for $\eta = 0.1$ (a) and $\eta = 0.2$ (b) and variable electronic coupling strength. The GR and the Redfield-theory results are given by the dashed and full lines, respectively. The potential-energy graph represents the donor (D) and acceptor (A) diabatic curves (full lines) and adiabatic curves (dashed lines) for strong (ω_0) and intermediate ($\omega_0/5$) values of $V_{\rm DA}$.

4.2 Ultrafast ET driven by wave-packet motion in the excited-state

Excitation of an ET system by a fs laser pulse generally prepares a wave packet in the excited state which can perform coherent vibrational motion. Effects of vibrational coherence in ultrafast ET processes have recently been observed experimentally in numerous systems, revealing the importance of strongly coupled underdamped system modes in ET dynamics [10, 18, 19, 25, 27–29, 31, 32].

In this section the dynamics of single-mode two-electronic-states ET models both in the normal as well as in the inverted regime is considered. Nonstationary initial conditions provide a nonequilibrium nuclear configuration of the donor electronic state at $t = 0$ and allow to observe ET driven by wave-packet motion in the initially excited state. Not only the population probability of the donor state, eq. (67), but also the wave packets themselves are monitored, using the coordinate representation of the RDM, projected on a relevant electronic state, eq. (A3).

4.2.1 Normal region

To investigate the effects of coherent wave-packet motion in the normal regime, the same system parameters as in section 4.1 are adopted, but with the preparation of a nonstationary initial state: it is assumed that the initial state is given by a vibrational ground-state wave packet located at the origin of the vibrational coordinate ($Q = 0$) in the upper diabatic potential. A moderate ET coupling ($V_{\mathrm{DA}} = 0.01\mathrm{eV}$) and weak damping ($\eta = 0.1$, $\omega_c = \omega_0$) have been assumed. Fig. 4 shows donor (D) and acceptor (A) potential-energy curves, time-dependent population probability of the donor diabatic state, $P_D(t)$, and the time evolution of the reduced density matrix in the coordinate representation, projected on the donor, $\sigma_D(Q,t)$, and acceptor, $\sigma_{\mathrm{A}}(Q,t)$, states. The wave-packet motion ($\sigma_{\mathrm{D}}(Q,t)$, $\sigma_{\mathrm{A}}(Q,t)$) is illustrated by three-dimensional (3D) and contour-plot views. The acceptor-state population probability is not shown, as it is trivially given by $1 - P_{\mathrm{D}}(t)$. All the graphs are combined

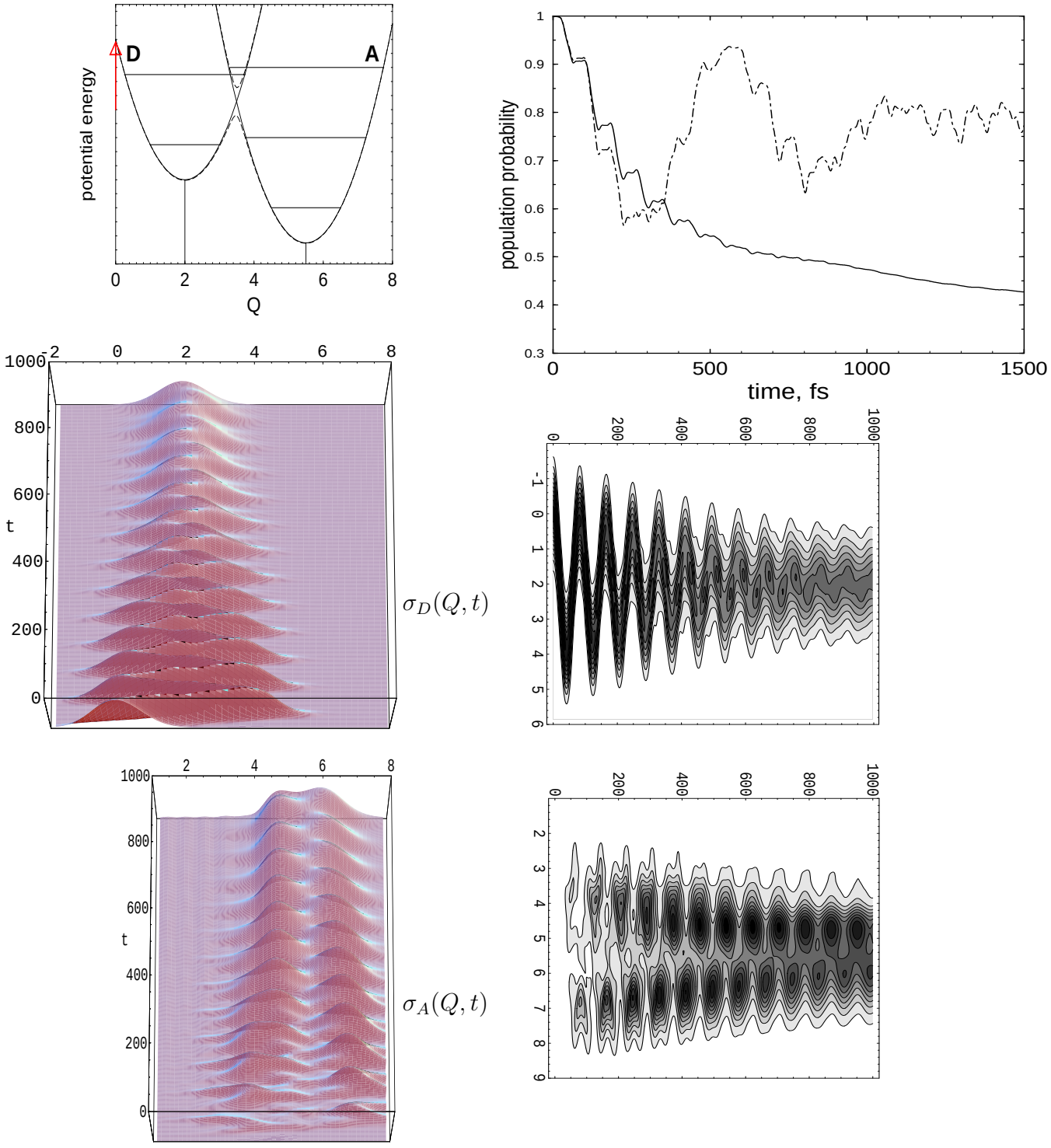

FIG. 4: Ultrafast ET in the normal region. The diabatic (solid lines) and adiabatic (dashed lines) potential-energy surfaces (the zero-oder vibrational states are indicated), the population probability of the diabatic donor state, $P_{\rm D}(t)$ (the dot-dashed curve represents the undamped, $\eta = 0$, system dynamics) and wave-packet motion in the donor, $\sigma_{\rm D}(Q,t)$, and acceptor, $\sigma_{\rm A}(Q,t)$, diabatic states in 3D and contour plots.

in the manner to provide either the same coordinate (potential-energy curves and 3D plots of $\sigma_{\rm D}(Q,t)$ and $\sigma_{\rm A}(Q,t)$) or the same time (population probability and contour plots of $\sigma_{\rm D}(Q,t)$ and $\sigma_{\rm A}(Q,t)$) scale.

The arrow in the PE-surfaces graph shows the location of the initial wave packet. It can be seen that the mean energy of the latter lies above the energy of the crossing point of the diabatic potentials, that is, the crossing point is accessible for the moving wave packet.

The dotted-dashed curve in the population-probability graph of Fig. 4 gives the result for $P_{\rm D}(t)$ without damping. The somewhat irregular beatings of the undamped system reflect electronic population oscillations (low-frequency beatings) and vibrational effects (high-frequency beatings). The quasi-periodic development of the undamped system demonstrates that there is no ET in the absence of damping.

The damped system exhibits an interesting and easily interpretable behavior. The initial system evolution is characterized by a step-like decay of $P_{\rm D}(t)$. The step structure reflects ET driven by coherent wave packet motion: a fraction of the wave packet is transferred to the product state each time the moving wave packet hits the crossing region. This interpretation is confirmed by the 3D and contour-plot graphs of the wave packet. In the donor state ($\sigma_{\rm D}(Q,t)$), a Gaussian wave packet, prepared by instantaneous excitation from the ground electronic and vibrational state, is driven to the minimum of the donor potential ($Q=2$) and its damped oscillations are clearly visible in 3D and contour-plot graphs. The wave-packet amplitude decreases because of the population transfer to the acceptor state.

The transfer of the population results in the wave-packet motion in the acceptor state ($\sigma_{\rm A}(Q,t)$ in Fig. 4). The wave packet appears in the vicinity of the crossing point of the diabatic potentials ($Q\simeq 3.5$) and oscillates towards the minimum of the acceptor potential ($Q=5.5$), gaining the amplitude from the donor state and being damped at the same time scale as $\sigma_{\rm D}(Q,t)$. The wave packets in the donor and acceptor states are out of phase, which leads to a double-peak structure of $\sigma_{\rm A}(Q,t)$.

Vibrational wave-packet motion is quenched after $\sim 600-800$ fs due to vibrational relaxation. The wave packet in the donor state being relaxed, the corresponding population

exhibits monotonous decay due to tunneling, analogous to Fig. 3. This long-time dynamics is also reflected in the intensity gain/loss in the $\sigma_{\rm A}(Q,t)/\sigma_{\rm D}(Q,t)$ contour plots.

4.2.2 Inverted region

We now turn to ET dynamics in the inverted region with nonstationary preparation. As a reference model, a single-mode model introduced previously by Wolfseder et al. [59] has been adopted. The system parameters are $\omega_0 = 0.064$ eV, $\Delta^{(\rm D)} = -2.0$, $\Delta^{(\rm A)} = -0.8281$, $\varepsilon_{\rm ad}^{(\rm D)} - \varepsilon_{\rm ad}^{(\rm A)} = 0.1259$eV, $V_{DA} = 0.01$ eV. The spectral function is given by eq. (30) with $\omega_c = \omega_0$ and $\eta = 0.4219$ which corresponds to the damping rate of the system oscillator $\Gamma = 0.01$ eV of Ref. [59]. The system-bath interaction is thus stronger than in the examples of sections 4.1 and 4.2.1. The diabatic and adiabatic potential-energy curves, the population probability of the initially prepared donor state, $P_D(t)$, and 3D and contour-plot graphs of the wave-packets in both diabatic electronic states, $\sigma_{\rm D}(Q,t)$, $\sigma_{\rm A}(Q,t)$ are shown in Fig. 5. As in the previous example, the same coordinate scale is used for potential-energy curves and 3D plots of $\sigma_{\rm D}(Q,t)$ and $\sigma_{\rm A}(Q,t)$, and the same time scale is chosen for the population probability and contour plots of $\sigma_{\rm D}(Q,t)$ and $\sigma_{\rm A}(Q,t)$. At $t = 0$, a Gaussian wave packet of appropriate width is placed on the donor diabatic potential at the origin of the vibrational coordinate. It is seen already from the PE graph, where the initial location of the wave packet is indicated by the arrow, that it will move periodically over the intersection point of the diabatic potentials.

The quasi-periodic dotted-dashed curve in the population-probability graph in Fig. 5 represents the dynamics of the undamped system ($\eta = 0$). It is similar to that of the normal region (Fig. 4) as it reflects a superposition of electronic and vibrational oscillations. Inclusion of damping results in the population dynamics given by the full line. We again observe ultrafast step-like initial ET driven by coherent wave-packet motion, which evolves into quasi-exponential decay after the quenching of the vibrational coherence at later times. However, in contrast to the normal region, ET is practically finished on the time scale of

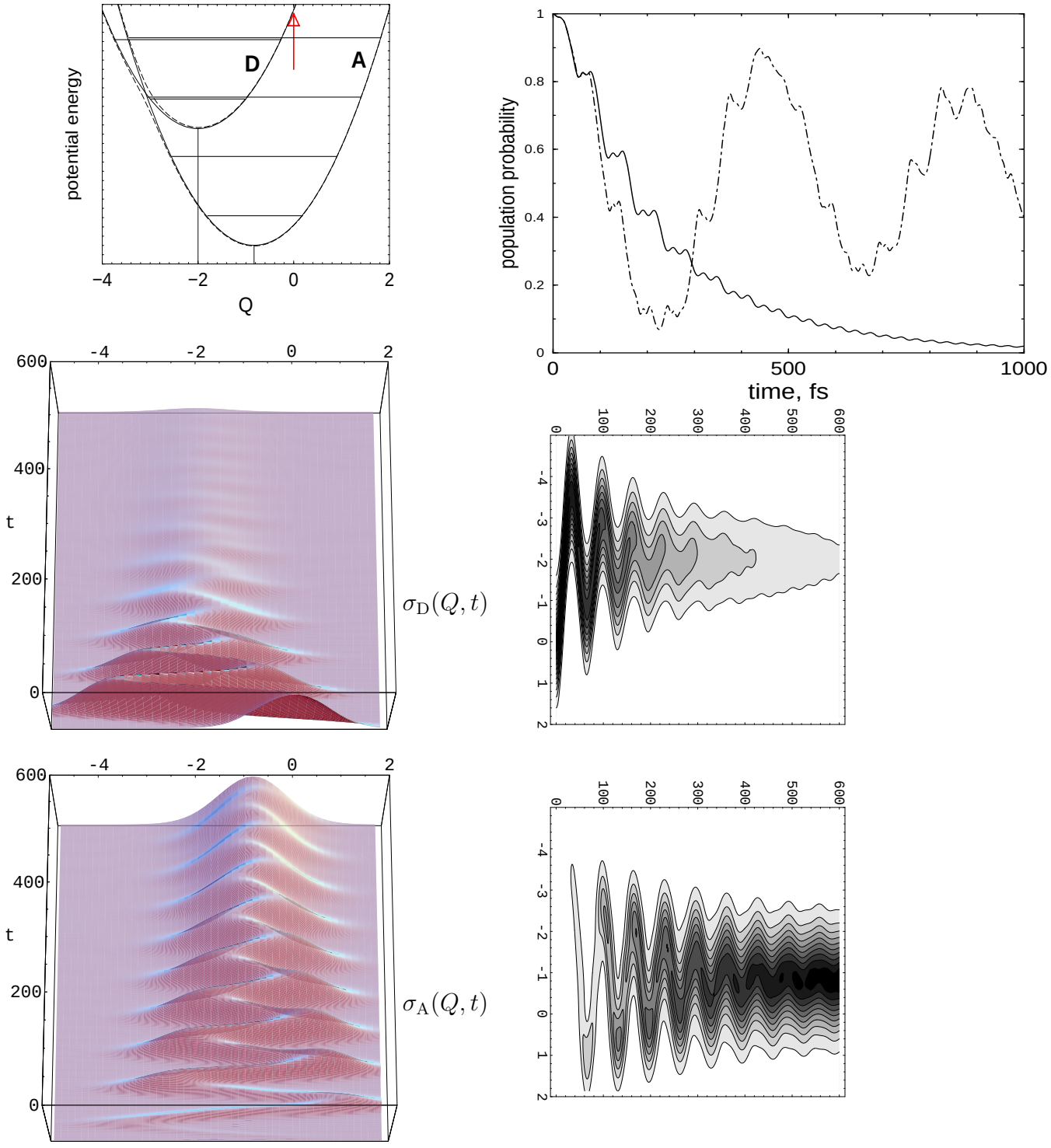

FIG. 5: Ultrafast ET in the inverted region. The diabatic (solid lines) and adiabatic (dashed lines) potential-energy surfaces (the zero-oder vibrational states are indicated), the population probability of the diabatic donor state, $P_{\rm D}(t)$ (the dot-dashed curve represents the undamped, $\eta = 0$, system dynamics) and wave-packet motion in the donor, $\sigma_{\rm D}(Q,t)$, and acceptor, $\sigma_{\rm A}(Q,t)$, diabatic states in 3D and contour plots.

the vibrational relaxation.

The initial vibrational amplitude of the donor-state wave packet, $\sigma_{\mathrm{D}}(Q,t)$, is the same as in the normal region, but the oscillations are damped faster because of the stronger system-bath coupling. The low barrier makes the crossing point accessible, even when the wave packet relaxes to the minimum of the donor potential, and, therefore, the population transfer is much more effective compared to the normal region.

The wave-packet motion in the acceptor state ($\sigma_{\mathrm{A}}(Q,t)$ in Fig. 5) is in phase with that in the donor state (constructive superposition). The damped oscillations, the gain in the intensity amplitude due to the electron transfer and relaxation to the ground vibrational state are clearly visible both in 3D and contour-plot graphs of $\sigma_{\mathrm{A}}(Q,t)$.

4.3 Performance of the secular approximation

Due to its numerical efficiency, the secular approximation (SA) to Redfield theory is very popular and often used in various applications. Though it can sometimes be acceptable (it has been successfully tested, e.g., for a ultrafast *cis-trans*-photoswitching model [83]), one has to be very cautious if the eigenstate spectrum is dense, so that the appearance of the non-strictly secular terms, satisfying the relation (43), is very probable.

The Redfield-theory modeling of ultrafast ET driven by vibrational wave-packet motion demonstrates a dramatic breakdown of the secular approximation. Fig. 6 shows the full Redfield-tensor (full line) and secular-approximation (dotted line) results for the population probability of the donor states for ET in normal (a) and inverted (b) regions. The system and damping parameters are as in sections 4.2.1 and 4.2.2, respectively. In the normal region, the characteristic effects of coherent vibrational motion are nearly completely lost in the SA, the quasi-stationary long-time tunneling rate, on the other hand, is accurately reproduced. The situation in the inverted region is even worse, than in the normal case: the SA calculations neither reproduce the fine structure, nor predict the correct overall decay rate.

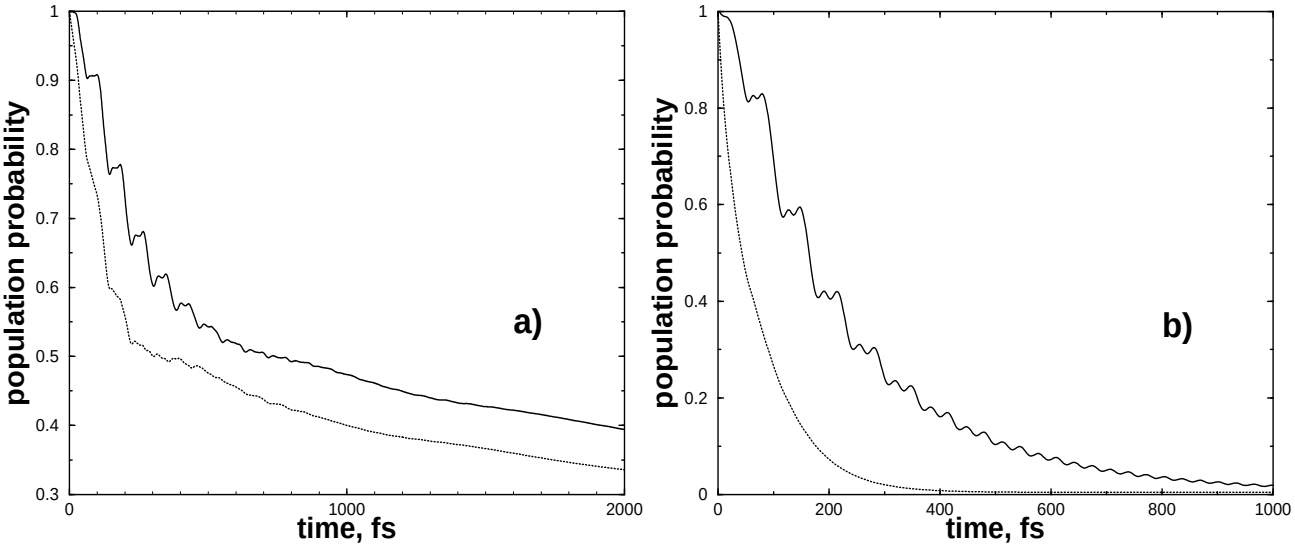

FIG. 6: Performance of the secular approximation for a model of ET, driven by vibrational wave-packet motion, in the normal (a) and inverted (b) regions. The SA and the full Redfield-tensor results are given by the dotted and solid lines correspondingly.

The exclusion of the non-strictly secular terms (43) from the standard SA equations of motion for the RDM (44), (45) is obviously responsible for the breakdown of the SA in Fig. 6. This can be proven if one performs calculations according to eq. (16), including only those Redfield-tensor elements which connect the terms with

$$|\omega_{\mu\nu} - \omega_{\kappa\lambda}| \lesssim \alpha,$$

where α is gradually increased from zero (standard or strict secular approximation) to a certain convergence value α_c, when all non-strictly secular terms are included. Such calculations for ET in the inverted region are shown in Fig. 7. The result for the population probability of the donor state is improving with increase of α and is converged for $\alpha_c = 0.05$eV (the corresponding curve cannot be distinguished from the full Redfield-tensor result in Fig. 7). As can be seen from eq. (43), the value of the convergence parameter α_c must be proportional to the Redfield tensor, that is, to the system-bath coupling strength. It means that the standard SA is expected to perform somewhat better for weaker system-bath interaction. The comparison of the SA results in the normal, η=0.1, and in the inverted, $\eta \simeq 0.4$, region in Fig. 6 confirms this expectation.

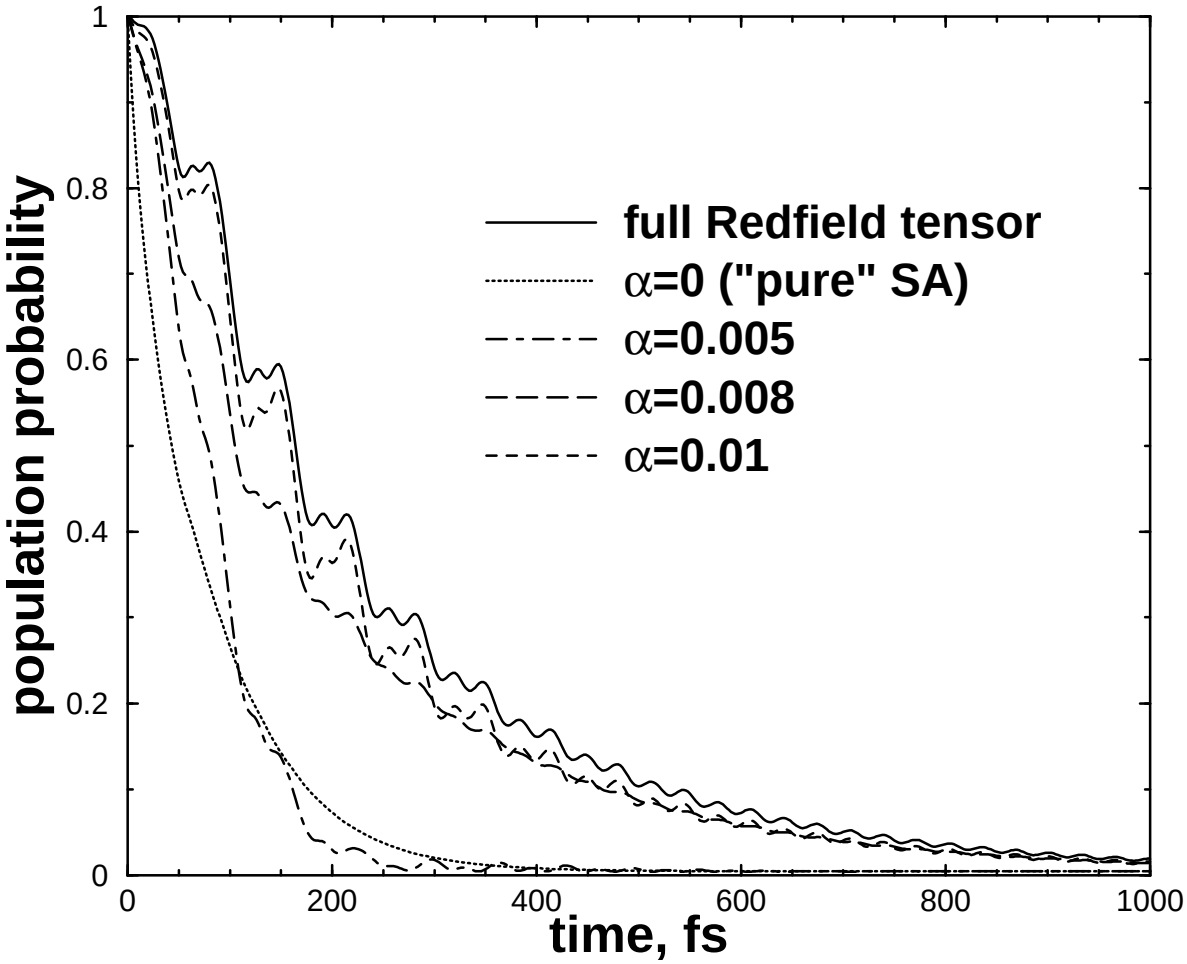

FIG. 7: The population probability of the donor state for ultrafast ET in the inverted region: a gradual improvement of the secular approximation due to inclusion of the non-strictly secular terms, (43), is illustrated.

The SA calculations for the normal region with stationary preparation (cf. section 4.1) in the weak-damping limit, η=0.1, are shown in Fig. 8 and are seen to be very accurate. Both the overall decay as well as the fine structures of the time-dependent populations are reliably reproduced. This reveals another specific feature of the SA applicability: the standard secular approximation performs rather well if coherent vibrational motion is not present in the system dynamics. In this case the neglect of couplings between coherences in the propagation of the density matrix, which is implied in the SA, does not introduce any significant error. It should also be noted here, that only a few levels are involved in the

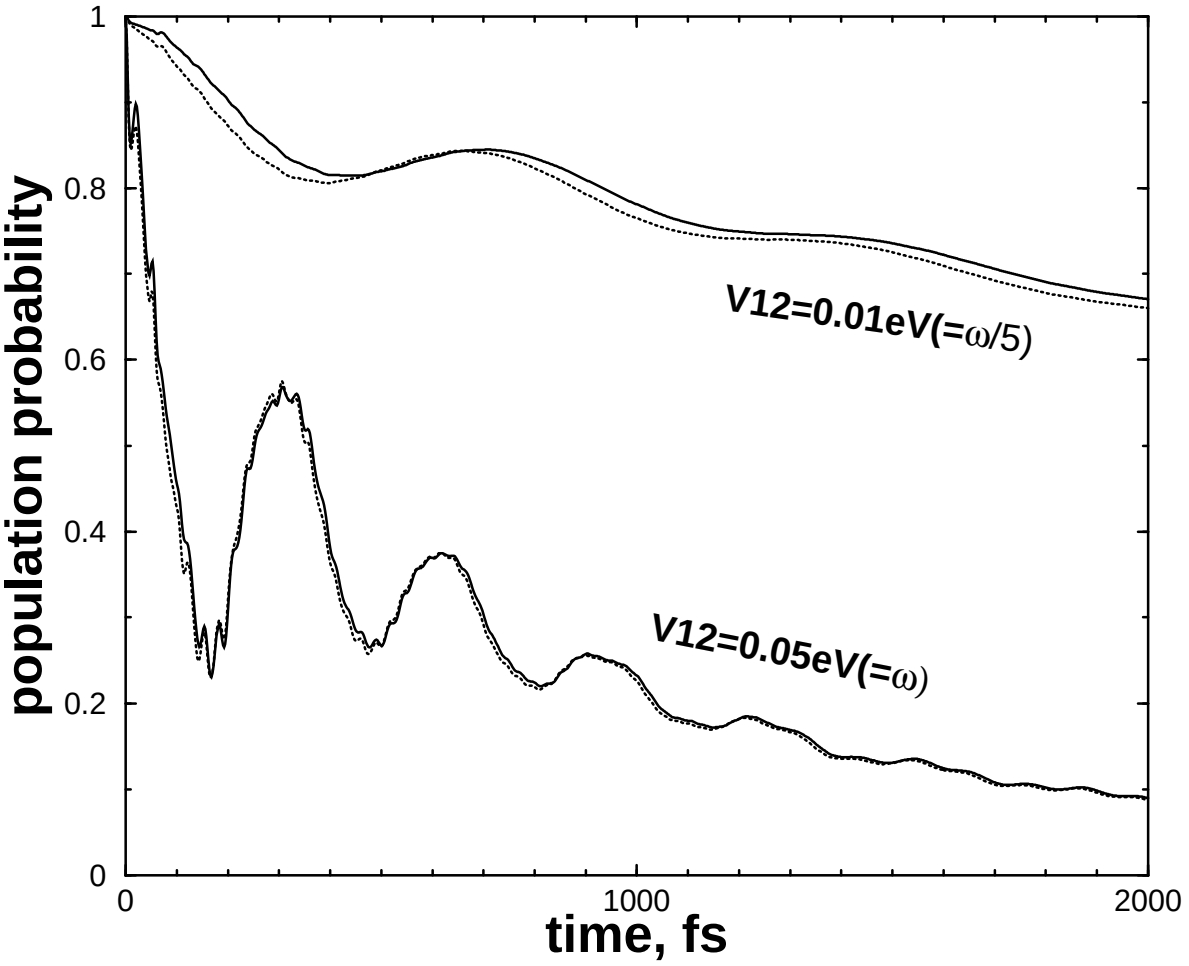

FIG. 8: Performance of the secular approximation for ET models with stationary preparation (section 4.1) for the intermediate and strong electronic coupling. The SA and full Redfield-tensor results are given by the dotted and solid lines respectively.

relaxational dynamics in the example of Fig. 8.

In principle, the relation $|R_{\mu\nu\kappa\lambda}|/|\omega_{\mu\nu}-\omega_{\kappa\lambda}|$ should be controlled for all combinations of eigenlevels in order to estimate the error introduced by the standard secular approximation. If there is a considerable number of terms with

$$\frac{|R_{\mu\nu\kappa\lambda}|}{|\omega_{\mu\nu}-\omega_{\kappa\lambda}|} \lesssim 1,$$

the standard SA must be avoided. This does not mean, however, that a full Redfield-tensor calculation is necessary. The inclusion of the non-strictly secular terms (43) is sufficient.

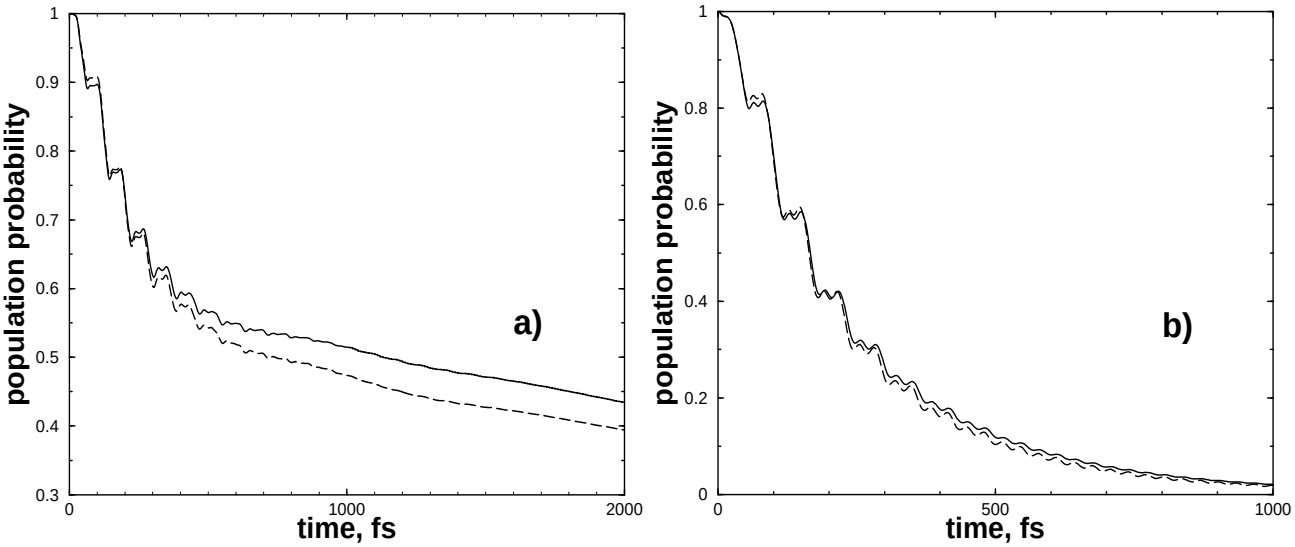

FIG. 9: Performance of the rotating-wave approximation for ET driven by vibrational wave-packet motion in the normal (a) and inverted (b) regions. The RWA and full Redfield-tensor results are given by dashed and solid lines, respectively.

4.4 Performance of the rotating-wave approximation and the diabatic-damping model

The performance of the rotating-wave approximation and the diabatic-damping model (sections 3.2, 3.3) compared to Redfield theory is briefly considered here for the models of ultrafast ET in normal and inverted regions introduced above (sections 4.2.1, 4.2.2). In contrast to the secular approximation, the RWA and DDM are not approximations which are specific for Redfield theory. The RWA is an approximate description of the linear system-bath coupling, provided both system and bath coordinates are harmonic, see eq. (55). As for the DDM, it has been employed to model ET processes and is similar to the standard Redfield theory as far as the system-bath interaction is concerned (perturbative treatment), but neglects the electronic coupling in the dissipation description and assumes the RWA expression for the system-bath coupling operator.

The Redfield-theory calculations with the full, eq. (24), and RWA, eq. (55), system-bath coupling operators are compared in Fig. 9 (the Redfield-tensor components are calculated according to eqs. (37) and (58), respectively). In both normal (Fig. 9a) and inverted (Fig. 9b)

ET regions, the RWA performs very well at short time scales. The coherent step structure, however, is washed out somewhat faster if the RWA is not assumed for H_{SB}. Due to this effect, the monotonous decay in the normal region starts slightly earlier, which causes a relatively minor deviation between the RWA and full-H_{SB} curves at later times in the normal region, Fig. 9a. The long-time decay rate, however, is correctly reproduced. Thus the RWA seems to be acceptable in the Redfield-theory formalism as its main effect is an effective reduction of the system-bath coupling strength.

Besides the RWA for the system-bath coupling H_{SB}, the diabatic-damping model implies the neglect of the electronic coupling in the relaxation-operator derivation for the ET modeling. Thus, by definition, the DDM is not suited for the description of the systems with larger values of the electronic coupling. Although, it is very attractive for numerical implementations, as it does not require the diagonalization of the system Hamiltonian and the Lindblad-form relaxation operator allows one to use a numerically effective Monte-Carlo propagation scheme.

Since the validity of the DDM has been extensively investigated elsewhere [61, 62], we do not consider it in detail here, but only point out that this approximation works perfectly for the models of ET driven by coherent wave-packet motion in the normal and inverted regions considered here (model parameter of sections 4.2.1 and 4.2.2), where the electronic coupling is of a moderate strength $V_{\mathrm{DA}} \leq \omega_0/5$. In order to demonstrate the expected deviations with the increase of the electronic coupling, Redfield-theory and DDM calculations for the model of section 4.1 (ET in the normal region with stationary preparation) are compared in Fig. 10 for $V_{\mathrm{DA}} = \omega_0/5$ and $V_{\mathrm{DA}} = \omega_0$. Thereby, the system-bath interaction operator of the form (60) has been used in the Redfield-theory calculations in order to be consistent with the DDM Hamiltonian. In the moderate electronic-coupling regime, $V_{\mathrm{DA}} = \omega_0/5$, the difference between the two curves can be hardly recognized, while the neglect of V_{DA} in the dissipation description in the strong electronic-coupling regime, $V_{\mathrm{DA}} = \omega_0$, results in a too strong damping of the electronic oscillations.

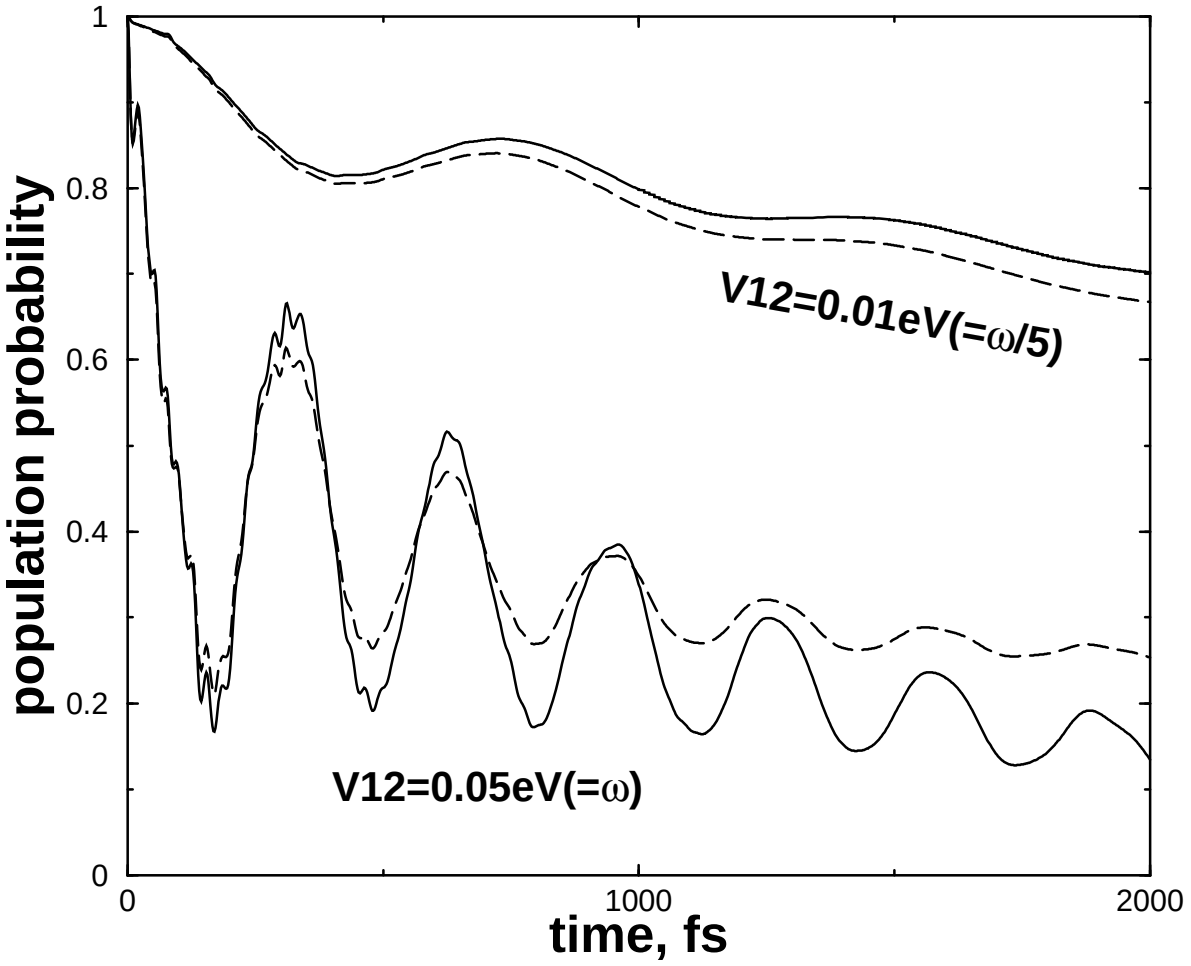

FIG. 10: Performance of the diabatic-damping model for an ET model with stationary preparation (section 4.1) for intermediate and strong electronic coupling, respectively. The DDM and full Redfield-tensor results are given by the dashed and solid lines respectively.

4.5 Wave-packet motion in the ground electronic state

Experimental evidence for wave-packet motion in the ground electronic state during an ultrafast ET reaction [18, 28, 32] has motivated us to extend our model in order to look at the population and wave-packet dynamics in the ground electronic state. The single-mode system Hamiltonian (50) including three diabatic electronic states has been chosen for the modeling of a back-electron-transfer reaction in the inverted region. An instantaneous excitation to a high-lying charge-transfer state with both nonstationary and stationary initial conditions is considered. The back-electron transfer to the ground state is modeled to occur

via an intermediate dark state. The diabatic charge-transfer (CT), intermediate (I) and ground (G) states are coupled to each other by $V_{\mathrm{CT,I}}$ and $V_{\mathrm{I,G}}$, respectively. The reaction-mode frequency is chosen as $\omega_0 = 0.05\mathrm{eV}$, and so is the bath cut-off frequency, $\omega_c = \omega_0$. The system-bath coupling parameter is varied to describe an effective damping of vibrational motion at the time scale of interest.

4.5.1 Non-stationary preparation

In this section we consider a model with the nonstationary initial condition, which is ensured by the coordinate displacement of the charge-transfer state with respect to the ground state, $\Delta_{\mathrm{CT}} = 2$. The position of the intermediate dark state is determined by $\Delta_{\mathrm{I}} = 1$. A moderate electronic coupling between the CT and intermediate states, as well as between the ground and intermediate states, has been chosen, $V_{\mathrm{CT,I}} = V_{\mathrm{I,G}} = \omega_0/5 = 0.01\mathrm{eV}$. The respective energetics of the diabatic states are $\varepsilon_{\mathrm{ad}}^{(\mathrm{CT})} - \varepsilon_{\mathrm{ad}}^{(\mathrm{G})} = 0.15\mathrm{eV}$, $\varepsilon_{\mathrm{ad}}^{(\mathrm{I})} - \varepsilon_{\mathrm{ad}}^{(\mathrm{G})} = 0.05\mathrm{eV}$. The system-bath coupling is relatively strong $\eta = 0.5$.

Fig. 11 shows the diabatic potentials for the system parameters chosen, the population probabilities of all three diabatic electronic states, $P_{\mathrm{CT}}(t)$, $P_{\mathrm{I}}(t)$, $P_{\mathrm{G}}(t)$, and the wave-packet motion in these states, $\sigma_{\mathrm{CT}}(Q,t)$, $\sigma_{\mathrm{I}}(Q,t)$, $\sigma_{\mathrm{G}}(Q,t)$ (in three-dimensional and contour-plot representations). As in Figs. 4, 5 (two electronic-state models), the graphs are combined to provide either the same coordinate or the same time scale. The location of the initial wave packet is indicated by the arrow in the potential-energy graph. The access of the crossing point is ensured by a sufficient excess in vibrational energy, provided by the initial condition.

The familiar step-structure (cf. population-probability graphs for two electronic-states models in Figs. 4, 5), caused by the nonstationary preparation is observed in the population decay of the CT state, $P_{\mathrm{CT}}(t)$, at early times. However, in contrast to the two-site inverted-region model (section 4.2.2, Fig. 5), the vibrational relaxation is completed earlier than the population transfer.

The population dynamics of the intermediate dark state reflects a competition between

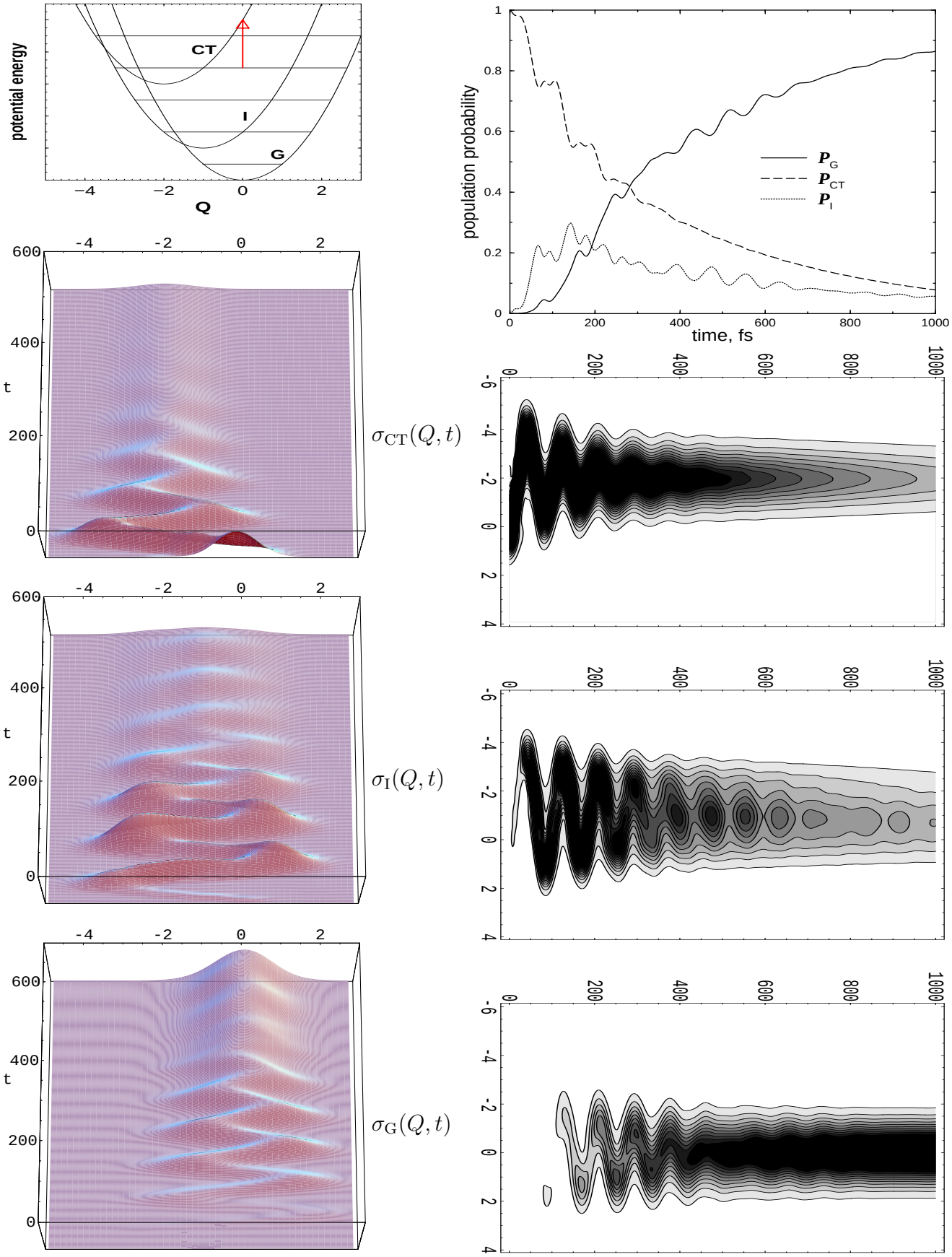

FIG. 11: Three electronic-state model for ultrafast back-ET in the inverted region with the non-stationary preparation. The diabatic potential-energy surfaces, the population probabilities of the charge-transfer, $P_{CT}(t)$, intermediate, $P_I(t)$, and ground, $P_G(t)$, electronic states, and wave-packet motion in these states, $\sigma_{CT}(Q,t)$, $\sigma_I(Q,t)$, $\sigma_G(Q,t)$ in 3D and contour plots.

a gain of the population from CT state and its loss to the ground electronic state. The population probability of this state, $P_{\mathrm{I}}(t)$, increases up to ~ 300 fs, but after this time the loss to the ground state is not longer compensated by the gain from the CT state.

The population probability of the ground state, $P_{\mathrm{G}}(t)$, shows a gain which is modulated, and the frequency of these modulations is the reaction mode frequency ω_0.

The coordinate representation of the RDM gives a clear picture of the wave-packet motion in every electronic state ($\sigma_{\mathrm{CT}}(Q,t)$, $\sigma_{\mathrm{I}}(Q,t)$, $\sigma_{\mathrm{G}}(Q,t)$ in Fig. 11). The wave packet in the CT state exhibits damped vibrational motion with a loss of the population to the intermediate dark state, and after $\sim$ 400 fs it is completely relaxed to the equilibrium position, $Q = -2$. The further population decay is monotonous, which can also be seen from the population probability graph ($P_{\mathrm{CT}}(t)$ after ~ 400 fs). The vibrational wave-packet motion in the intermediate state,$\sigma_{\mathrm{I}}(Q,t)$, survives at the same time scale as in the CT state.

At $t \simeq 100$ fs coherent wave-packet motion in the ground state becomes visible. The initial amplitude of the oscillations is determined by the location of the crossing of the ground state with the intermediate state and is slightly smaller than that in the CT and dark states. The oscillations are efficiently damped at ~ 400 fs time scale, but small-amplitude vibrational motion survives up to ~ 800 fs (see the contour plot of $\sigma_{\mathrm{G}}(Q,t)$ in Fig. 11). This gives rise to the oscillatory structure in population probability of the ground and intermediate states, $P_{\mathrm{I}}(t)$, $P_{\mathrm{G}}(t)$, between ~ 400 fs and ~ 800 fs, as the crossing point of these states is still accessible for the slightly moving wave-packet. It is interesting to note, that rather considerable modulations of the population probability are possible due to tiny vibrations.

4.5.2 Stationary preparation

In contrast to the model of section 4.5.1, we consider here a situation without coordinate shift between the initial CT and the ground electronic states, $\Delta_{\mathrm{CT}} = 0$, corresponding to the stationary initial condition. As a consequence, no moving wave-packet is prepared in the initial electronic state. The displacement of the intermediate state, $\Delta_{\mathrm{I}} = -2$, and the

respective vertical shifts of the PE functions, $\varepsilon_{\rm ad}^{\rm (CT)} - \varepsilon_{\rm ad}^{\rm (G)} = 5\omega_0 = 0.25$eV, $\varepsilon_{\rm ad}^{\rm (I)} - \varepsilon_{\rm ad}^{\rm (G)} = 3\omega_0 = 0.15$eV, allow a barrierless transfer from the CT to the intermediate state (see Fig 12). The electronic couplings are rather substantial, compared to the system frequency ($\omega_0 = 0.05$eV), $V_{\rm CT,I} = 0.03$eV, $V_{\rm I,G} = 0.02$eV. There is no excess in vibrational energy in the initially prepared electronic state (stationary preparation), and the coupling to the bath, η =0.15, is weaker than in the case of the nonstationary initial condition.

The diabatic PE functions, the population probabilities of the three diabatic states, $P_{\rm CT}(t)$, $P_{\rm I}(t)$, $P_{\rm G}(t)$, as well as the projections of the coordinate representation of the RDM to the intermediate and dark states, $\sigma_{\rm I}(Q,t)$, $\sigma_{\rm G}(Q,t)$, are shown in Fig. 12. The CT-state projection is not shown, as no wave-packet motion is expected in this state due to the stationary initial condition. The same coordinate/time scale of the graphs helps to follow the system dynamics.

Similar to the donor-state population of the two electronic-states model for ET in the normal region with stationary preparation (section 4.1), the population probability of the CT state, $P_{\rm CT}(t)$, exhibits electronic oscillations due to the nonadiabatic coupling $V_{\rm CT,I}$, which are damped on a time scale of about 400 fs. A considerable gain in the intermediate-state population, $P_{\rm I}(t)$, is observed at $t \simeq$50 fs and is followed by a step-like decay. These steps, which are also reflected in the increasing population of the ground electronic state ($P_{\rm G}(t)$), can be interpreted as being due to the presence of vibrational wave-packet motion in this case. This is confirmed by the $\sigma_{\rm I}(Q,t)$ and $\sigma_{\rm G}(Q,t)$ 3D and contour-plot graphs. Appearing in the vicinity of the crossing point with the CT potential ($Q = 0$), the wave-packet in the intermediate state, $\sigma_{\rm I}(Q,t)$, is strongly driven to the minimum of the corresponding potential ($Q = -2$) and disappears rapidly because of the back transfer to the ground state.

The oscillations in the ground state appear at about 100 fs. The damped vibrational motion and relaxation to the ground state at about 1000 fs are nicely illustrated by 3D and contour plots of $\sigma_{\rm G}(Q,t)$. Despite the stationary preparation, the pronounced vibrational motion is observed in the ground electronic state which is driven by the back-ET reaction.

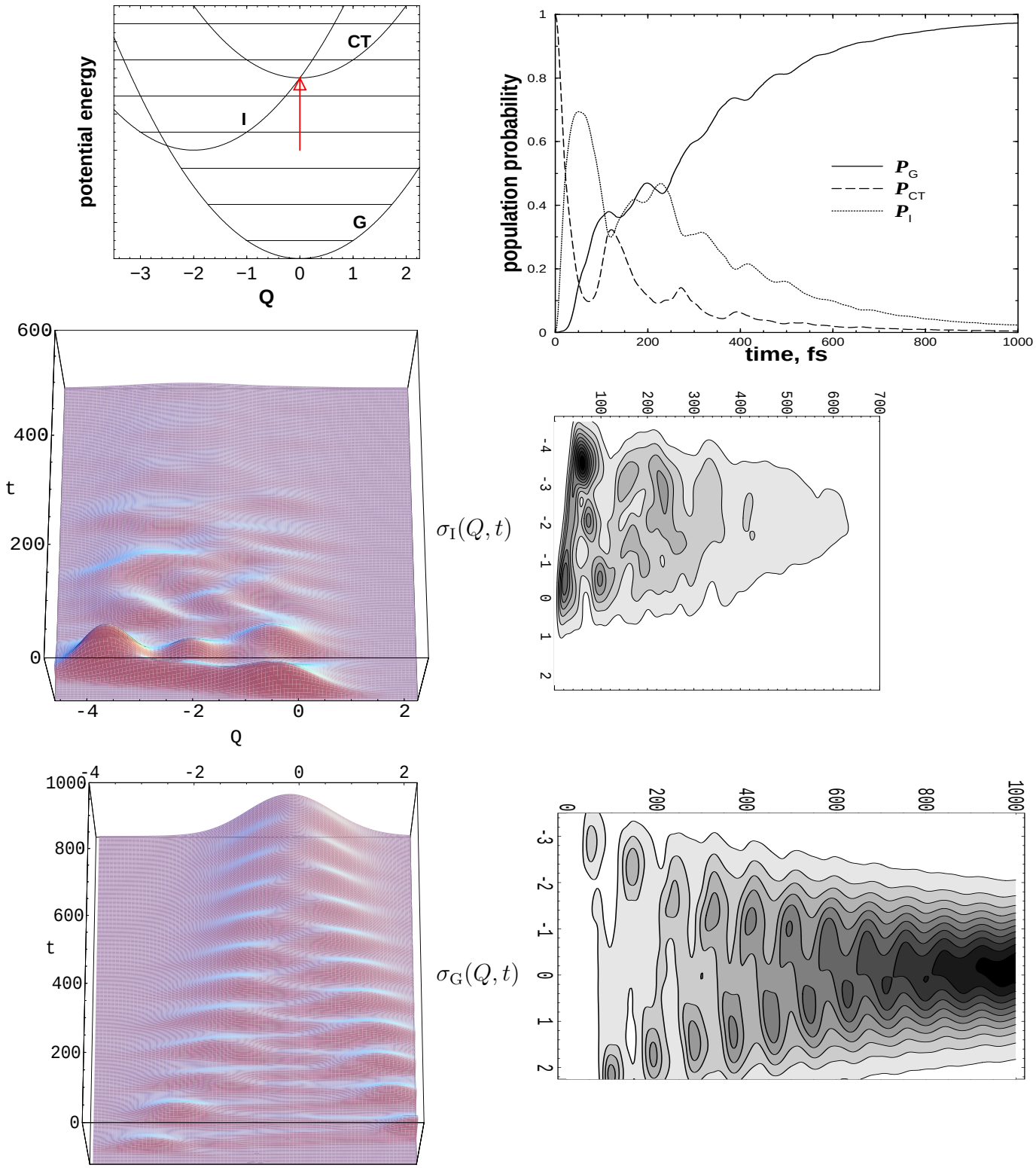

FIG. 12: Three electronic-state model for ultrafast back-ET in the inverted region with the stationary preparation. The diabatic potential-energy surfaces, the population probability of the charge-transfer, $P_{\rm CT}(t)$, intermediate, $P_{\rm I}(t)$, and ground, $P_{\rm G}(t)$, electronic states, and wave-packet motion in these states, $\sigma_{\rm CT}(Q,t)$, $\sigma_{\rm I}(Q,t)$, $\sigma_{\rm G}(Q,t)$ in 3D and contour plots.

Wave-packet motion does not accelerate the reaction in this case as it is not present in the initial CT state, but it can be observed in the ground electronic state after a certain delay time as a satellite of back ET. One could imagine longer delay times if there are more intermediate states involved in the reaction.

5. INVESTIGATION OF THE VALIDITY OF REDFIELD THEORY FOR THE MODELING OF ULTRAFAST ELECTRON TRANSFER

Being perturbative with respect to the system-bath interaction, Redfield theory may be applied only to weakly damped systems. In order to investigate its validity for the models of ultrafast ET introduced above, a comparison with numerically exact calculations has been performed for several illustrative models, characterized by different system parameters, the system-bath coupling strength being varied for each of them. The results, obtained within the recently developed self-consistent hybrid approach [63] have been used as a reference. No additional approximations have been involved in the Redfield-theory formalism in order to be consistent with the exact calculations. That is the linear system-bath coupling has been defined without the RWA, eq. (24), and the renormalization term has been added to the system Hamiltonian, as required by the inclusion of the imaginary part of the Redfield tensor in the description of dissipation.

The Redfield-theory calculations have been performed both with time-dependent and time-independent Redfield tensor, which allows us to discuss the validity of the stationary Redfield-tensor approximation for different ET models.

Like in sections 4.1 and 4.2, a two-site single-mode system Hamiltonian is adopted for the ET modeling, the two electronic states correspond to the donor and acceptor state, respectively. An instantaneous excitation from the ground electronic state, which is not explicitly included in the system Hamiltonian, to the donor state is assumed. The initial condition is referred to as stationary, if there is no coordinate displacement between the ground and initially excited electronic states, and as nonstationary otherwise.

The reaction mode frequency is chosen as $\omega_0 = 0.05$ eV in all examples. If it is not discussed explicitly, the bath cut-off frequency is equal to the system mode frequency, $\omega_c = \omega_0 = 0.05$ eV, and the temperature is zero, $T = 0$. The population probability of the initially excited state (67), calculated within Redfield-theory (RT) and self-consistent hybrid approach (SHA), is monitored for different values of the system-bath coupling constant η.

5.1 Self-consistent hybrid approach

To investigate the validity of Redfield theory for electron transfer reactions, numerically exact reference results are required. For this purpose we have applied the self-consistent hybrid approach, which has been proposed recently for simulating quantum dynamics in the condensed phase[63, 66]. The method as well as applications to different electron-transfer systems have been described in detail in Refs. [63, 66, 98]. Here we briefly introduce the general idea and give some details specific to the applications in this work.

The self-consistent hybrid method is based on an iterative convergence procedure for a dynamical hybrid approach. After a discretization of the bath, which for the examples considered in this work usually requires between 30 and 120 modes (depending on the specific parameters under consideration and the time scale of interest), the overall system is partitioned into a 'core' and a 'reservoir'. The former is treated via a high level quantum mechanical method and the latter is treated via a more approximate method. For the applications in this work we have used the MCTDH method [99–101] for the core (which allows us to treat a rather large system quantum mechanically) and classical mechanics for the reservoir. Accordingly, the core comprises the two electronic states, the reaction coordinate, as well as vibrational bath modes with frequencies $\omega > \tilde{\omega}$, where $\tilde{\omega}$ serves as a convergence parameter. The reservoir comprises the remaining low frequency modes ($\omega < \tilde{\omega}$). As described in detail in Ref. [63], a sensible initial guess for $\tilde{\omega}$ can be obtained using a thermal criterion. Test calculations are then carried out and the number of bath modes included in the core (as well as other variational parameters) is increased systematically until convergence (usually to within 10% relative error) is reached. If all the bath modes were treated classically (i.e. the core comprised only the electronic two-state system) this method would be equivalent to the classical path (Ehrenfest) method. But because the calculation is converged with respect to the number of bath modes included in the quantum propagation, the results are numerically exact.

It is noted, that the models considered in this work are characterized by a relatively high

frequency of the reaction coordinate and a fast time scale of the bath. As a consequence, the classical treatment of low-frequency modes of the reservoir is not efficient for very low temperature. Therefore, in most of the calculations for $T = 0$ K all bath modes have been treated by the MCTDH method, corresponding to the full-core limit. This finding is in contrast to previous applications of the method [63, 66, 98], and indicates that the low frequency modes of the reservoir have little dynamical impact on the overall electron transfer dynamics in the model systems considered here.

5.2 Normal region

Three different models for the ET in the normal region are considered. Two of them have been already discussed in sections 4.1 and 4.2.1, the third one is a zero-bias or symmetric model.

5.2.1 Symmetric case

The symmetric or zero-bias model is characterized by symmetrical coordinate and vertical displacements of the system diabatic potentials. The coordinate shifts $\Delta_{\mathrm{A,D}} = -\kappa_{\mathrm{A,D}}/\omega_0 = \pm 1$ and zero energy bias, $\varepsilon_{\mathrm{D}} = \varepsilon_{\mathrm{A}}$, define essentially a two-level model in the low-temperature regime. The initial preparation is non-stationary, as the ground-state minimum is assumed to be centered at the origin of the coordinate scale. The electronic coupling is rather small compared to the system frequency, $V_{\mathrm{DA}} = \omega_0/10 = 0.005$ eV. Therefore, the adiabatic potentials can be hardly distinguished from the diabatic potentials in the potential-energy graph of Fig. 13, which also shows the population probability of the initially excited diabatic electronic state for the system-bath coupling parameters $\eta = 0$ (a), $\eta = 0.1$ (b) and $\eta = 0.5$ (c). The solid lines in the population-probability graphs are the results of numerically exact SHA calculations, the dotted and dashed lines represent Redfield-theory results with time-dependent and stationary (time-independent) Redfield tensor, respectively.

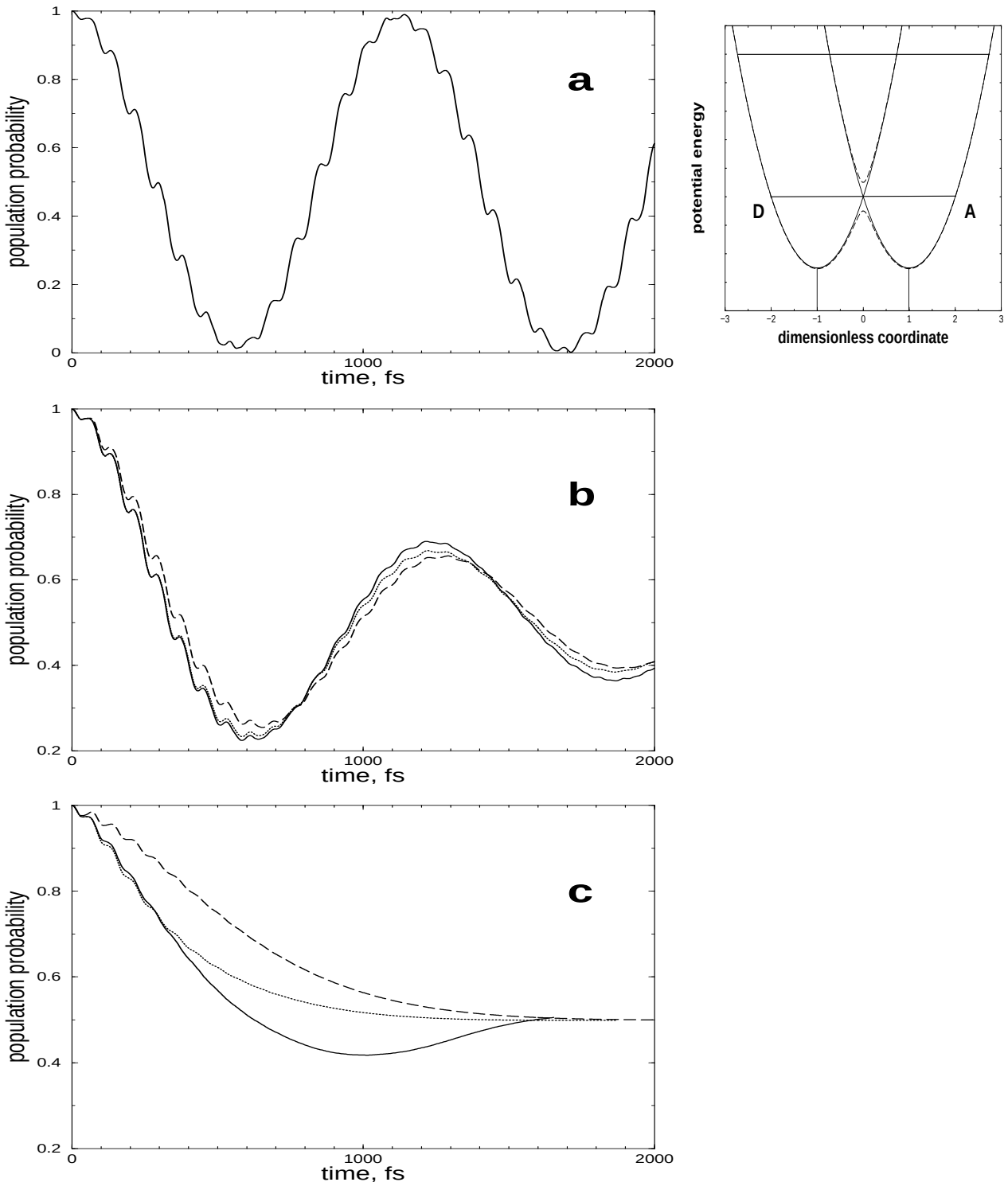

FIG. 13: Normal region, symmetric case: the population probability of the initially excited electronic state for (a) $\eta = 0$, (b) $\eta = 0.1$, (c) $\eta = 0.5$. The Redfield results, calculated with the stationary and time-dependent Redfield tensor, are the dashed and dotted curves, respectively. The solid line corresponds to the exact SHA calculations.

The undamped system dynamics, $\eta = 0$ (Fig. 13a), is characterized by long-period oscillations due to the electronic coupling. The nonstationary preparation results in vibrational motion in the reaction mode, which is reflected in the population dynamics as higher-frequency modulations of the electronic oscillations. The damped system dynamics is shown in Fig. 13b ($\eta = 0.1$) and Fig. 13c ($\eta = 0.5$). The coupling to the bath causes the damping of both types of oscillations and relaxation to the equilibrium population distribution. As expected, the accuracy of the RT results deteriorates with the increase of η. In the case of small system-bath coupling (Fig. 13b), the RT results are in perfect agreement with the exact calculations on a ps time scale. With the increase of the coupling (Fig. 13c), the Redfield results are acceptable only at a shorter (about 300 fs) time scale. The calculations with the stationary Redfield tensor provide much less satisfactory results (dashed lines in population-probability graphs in Fig. 13).

There are essentially only two eigenstates E_1, E_2 with rather small eigenfrequency, $\omega_{12} = E_1 - E_2$, involved in the system dynamics. Due to the low frequency in the exponent, the time integrals in the Redfield-tensor elements, (34), converge to their stationary values very slowly and the stationary Redfield-tensor approximation is not fulfilled. The convergence can be accelerated by an increase of the bath cut-off frequency ω_c, as this reduces the bath correlation time τ_c. To investigate the ω_c-dependence of the stationary Redfield-tensor approximation, calculations for different values of ω_c are compared in Fig. 14 on a shorter time scale. The value of $\eta\omega_c$ is kept constant to insure the same renormalization of the PE surfaces due to the system-bath interaction. An intermediate damping strength, $\eta = 0.3$, for the case of $\omega_c = \omega_0$ has been chosen as a reference. As expected, the difference between stationary and nonstationary Redfield-tensor results decreases with the increase of ω_c. For a small $\omega_c = \omega_0/5$, the deviation between the two RT curves is very large, and even time-dependent Redfield-tensor calculations cannot be reliable, as the effective value of the system-bath coupling parameter, $\eta = 1.5$, is far too large. For $\omega_c = \omega_0$, the agreement between time-dependent Redfield-tensor and SHA results is very good and the difference between the two RT curves is less pronounced. It reduces even more for a larger cut-off

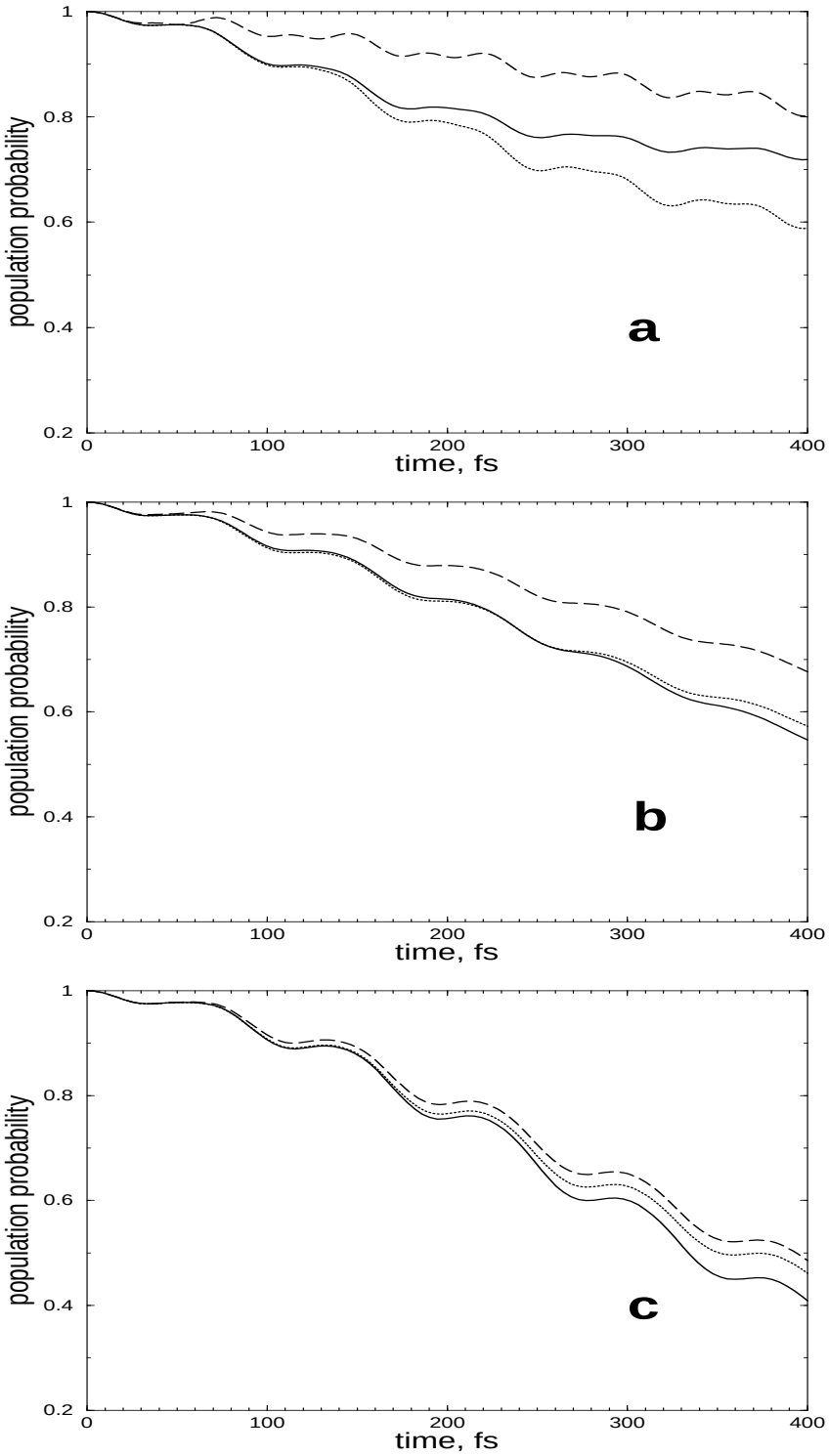

FIG. 14: Normal region, symmetric case: the population probability of the initially excited electronic state for (a) $\omega_c = \omega_0/5$, $\eta = 1.5$, (b) $\omega_c = \omega_0$, $\eta = 0.3$ and (c) $\omega_c = 5\omega_0$, $\eta = 0.06$. The Redfield results, calculated with the stationary and time-dependent Redfield tensor, are the dashed and dotted curves, respectively. The solid line corresponds to the exact SHA calculations.

frequency, $\omega_c = 5\omega_0$.

5.2.2 Asymmetric case, nonstationary preparation

This model has been considered in section 4.2.1 as an example of the normal region-ET, driven by wave-packet motion in the reaction mode. The coordinate displacements of the potentials are defined by $\Delta_{\mathrm{D}} = 2$ and $\Delta_{\mathrm{A}} = 5.5$, the ground electronic state being located at the coordinate origin. The adiabatic energy gap is 0.045 eV and electronic coupling is of intermediate strength, $V_{\mathrm{DA}} = \omega_0/5 = 0.01$ eV.

The potential-energy profiles and the population dynamics of the donor state for $\eta = 0$ (a), $\eta = 0.1$ (b) and $\eta = 0.5$ (c) and $T = 0$, as well as for finite temperature, $T = 300$ K and $\eta = 0.1$ (d) are shown in Fig. 15.

The system dynamics without coupling to the bath (Fig. 15a) is of the same nature as in the symmetric case (Fig. 13a), but the frequency ratio of both type of oscillations is different due to the stronger V_{DA}. However, there is no electronic back-flow already for a small system-bath coupling, $\eta = 0.1$, Fig. 15b, in contrast to the previously considered example (cf. Fig. 13b). This is caused by the fast vibrational relaxation in the acceptor state and the relatively high barrier. The coherent wave-packet motion, reflected by the step-like decay of the donor-state population probability, has been discussed in detail in sections 4.2.1, 4.2.2.

The increase of the coupling parameter, η =0.5 (Fig. 15c), results in a slower population decay as coherences are washed out faster and vibrational relaxation in the donor state slows down the ET.

The Redfield-theory approach appears to reproduce excellently the exact calculations for the previously considered weak-coupling regime, $\eta = 0.1$. As for the larger value η =0.5 (Fig. 13c), RT results coincide with those of SHA only up to 120 fs. After this time, they reproduce well the step-structure, but predict a slower decay.

The difference between stationary and nonstationary Redfield-tensor results is relatively

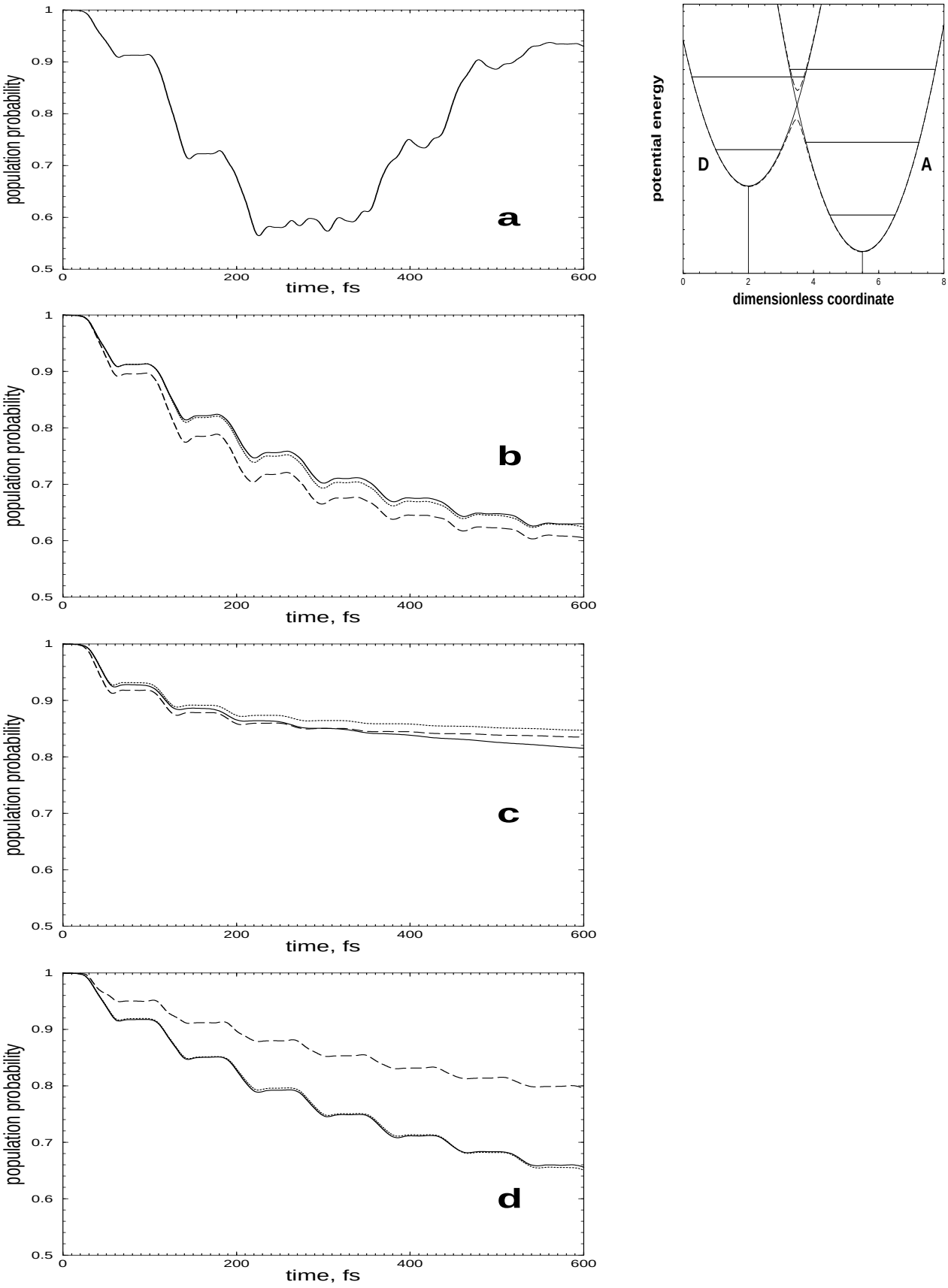

FIG. 15: Normal region, asymmetric case, nonstationary preparation: the population probability of the initially excited electronic state for (a) $\eta = 0$, (b) $\eta = 0.1$, (c) $\eta = 0.5$ and (d) for $\eta = 0.1$ and $T = 300$K. The Redfield calculations with the stationary and time-dependent Redfield tensor, are the dashed and dotted curves, respectively. The solid line corresponds to the exact SHA results.

small in Figs. 15 b,c, but can become much more pronounced for finite-temperature calculations. As an example, Fig. 15d shows simulations for $T = 300K$ (η =0.1). As was mentioned in section 2.5, the absolute values of the Redfield tensor elements increase with temperature, especially in the region of small eigenfrequencies. Furthermore, the non-zero temperature can slow down the convergence of some time integrals in (34). This is the case for integrals with negative eigenfrequencies Ω, corresponding to transitions with energy increase caused by thermal fluctuations. These factors accumulate the error introduced by the stationary Redfield-tensor approximation and it performs worse compared to the zero-temperature case.

It is interesting to compare here the donor-state population dynamics, obtained for the same damping parameters as in section 4.2.1 ($\eta = 0.1$, $\omega_c = \omega_0$) with the previous results, calculated neglecting the imaginary part of the Redfield tensor in the relaxation description. The comparison is shown in Fig. 16. The solid line is the Redfield-theory result with time-independent Redfield tensor, the renormalization term being added to the system Hamiltonian and the imaginary part of the Redfield tensor being taken into account. The dotted line reproduces the result of the model calculations as in chapter 4 (but without RWA for the system-bath coupling operator), the Lamb shift being neglected.

The population (electron) transfer is seen to be somewhat less effective when the imaginary part of the Redfield tensor is taken into account, and the long-time tunneling rate is considerably reduced. This could mean that the renormalization of the potential-energy surfaces enlarges the barrier height to some extent.

5.2.3 Asymmetric case, stationary preparation

In this model example, the geometry of the diabatic PE surfaces is the same as in the previous case of the nonstationary preparation, section 5.2.2. However, there is no shift between the ground state and donor state minima (stationary preparation). The validity of the GR formula has been tested for this model in section 4.1, the electronic coupling V_{DA} being varied. Here we chose a rather strong value $V_{\mathrm{DA}} = \omega_0 = 0.05$ eV, and concentrate on

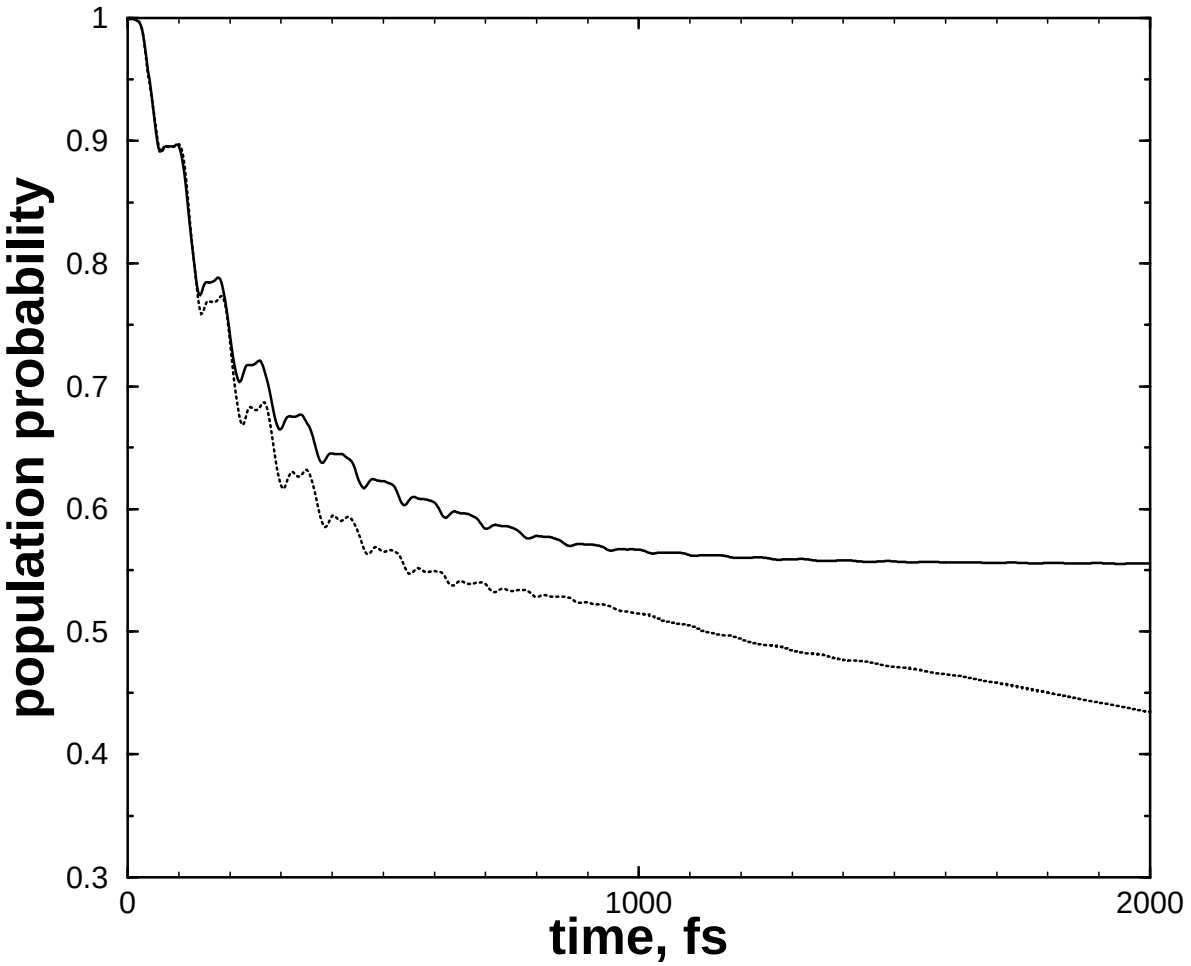

FIG. 16: Normal region, asymmetric case, non-stationary preparation: the population probability of the initially excited electronic state for $\eta = 0.1$, Redfield-theory calculations with the time-independent Redfield tensor. Solid line: the imaginary part of the Redfield tensor is taken into account and the renormalization term is added to the system Hamiltonian. Dotted line: the imaginary part of the Redfield tensor is neglected, no renormalization term in the system Hamiltonian.

the performance of Redfield theory.

RT and DHA results for the donor-state population probability, as well as the diabatic and adiabatic potential-energy curves, are shown in Fig. 17. The strong electronic coupling lowers considerably the barrier, but the adiabatic potential has still a double-well structure. The strong V_{DA} is also responsible for higher-frequency modulations of the electronic oscillations of the undamped system in Fig. 17a: The excess of vibrational energy in the excited state is caused by a significant difference between the initially prepared vibrational state and

the eigenstates of the lower adiabatic potential. In the small system-bath coupling regime, $\eta = 0.1$ (Fig. 17b), the electronic oscillations survive for about 1000 fs. RT performs rather well in this case. The exact calculations are precisely reproduced up to 150 fs, and qualitatively well after this time. The stronger damping case, $\eta = 0.5$, shows quasi-exponential decay after some more complicated initial dynamics (Figs. 17c). The Redfield results are in reasonable agreement with the exact calculations for approximately 400 fs, but decay to negative values at longer time. The stationary Redfield-tensor approximation performs much better in this example compared to the previous ones. Stronger electronic coupling enlarges the eigenstate frequencies and provides faster convergence of the time integrals in the Redfield-tensor components (34).

The decay of the donor-state population probability to negative values for $\eta = 0.5$ disappears for finite temperature of the bath. Fig. 18 shows the time-dependent Redfield-tensor calculations for $T = 0$ (solid line), $T = 30$ K (dashed line), $T = 90$ K (dotted-dashed line) and $T = 300$ K (dotted line). The long-time result improves with the increase of temperature, providing positive values of $P_{\mathrm{D}}(t)$ for $T = 90$ K and $T = 300$ K.

It is worth mentioning here, that if the imaginary part of Redfield tensor is neglected, a correct Boltzmann distribution is obtained in the long-time limit $t \to \infty$, as it is provided by the definition of the real parts of the Redfield-tensor.

5.3 Inverted region

The ET in the inverted region is found to be particularly fast and effective. The displacements $\Delta_{\mathrm{D}} = -2$ and $\Delta_{\mathrm{A}} = -1$, and adiabatic energy gap of 0.1 eV provide a very low barrier, and the crossing point is easily accessible for the wave-packet prepared in the upper electronic state (the ground electronic state is assumed not to be displaced from the coordinate origin, i.e., non-stationary preparation, see Fig. 19).

The diabatic and adiabatic potential-energy curves, as well as the time-dependent population probability of the donor electronic state for $\eta = 0$ (a), $\eta = 0.1$ (b), $\eta = 0.5$ (c), and

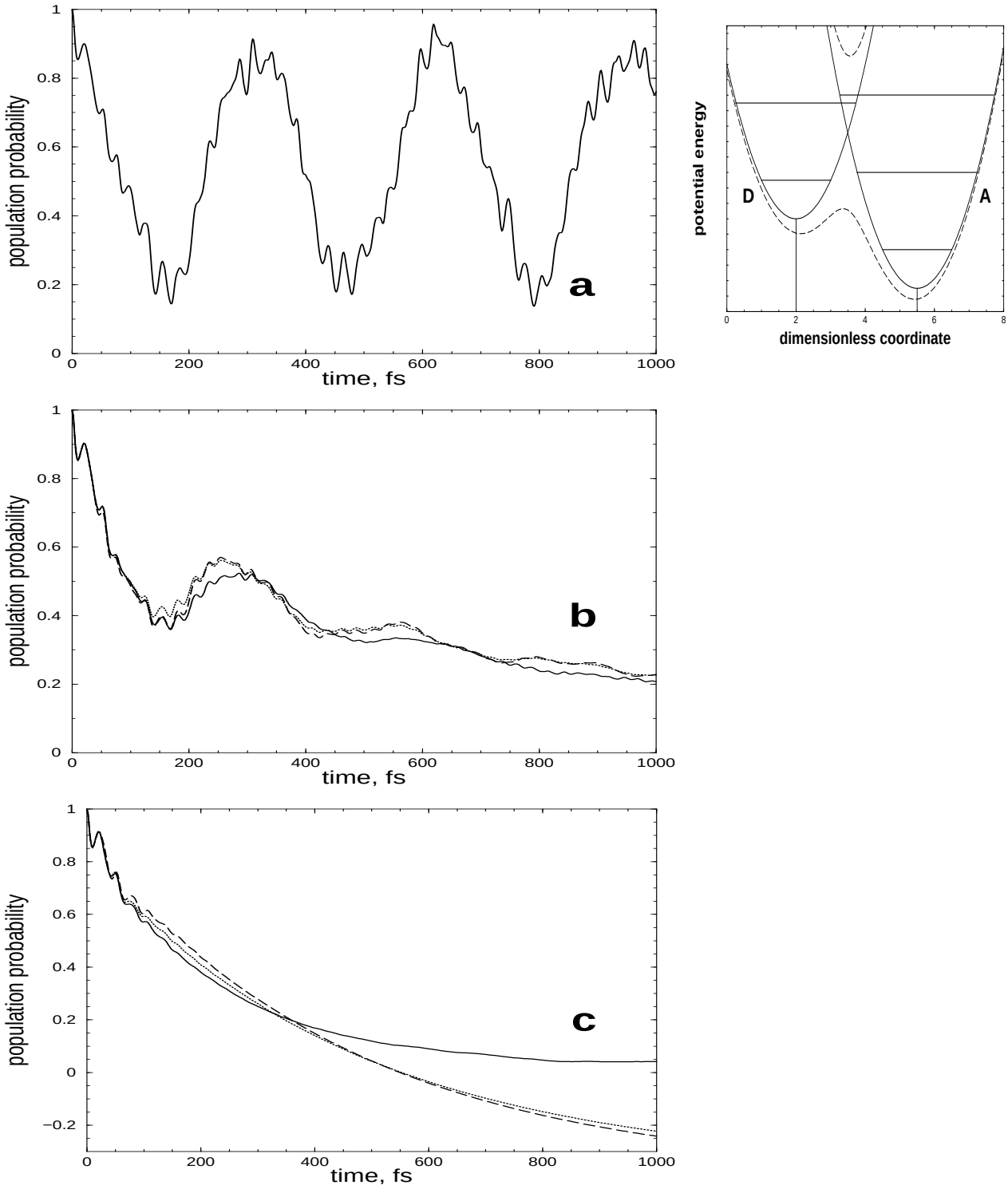

FIG. 17: Normal region, asymmetric case, stationary preparation: the population probability of the initially excited electronic state for (a) $\eta = 0$, (b) $\eta = 0.1$, (c) $\eta = 0.5$. The Redfield results, calculated with the stationary and time-dependent Redfield tensor, are the dashed and dotted curves, respectively. The solid line corresponds to the exact SHA calculations.

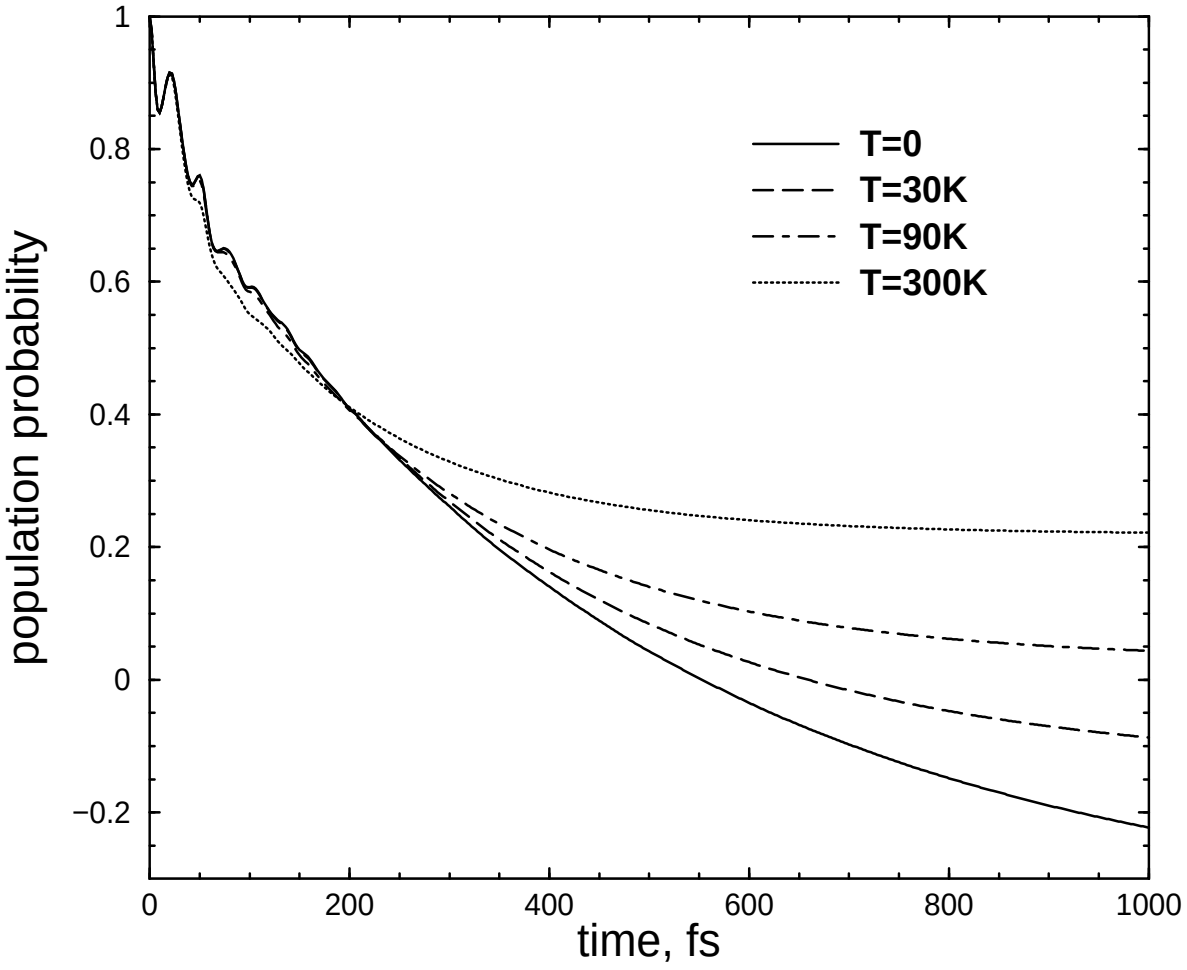

FIG. 18: Normal region, asymmetric case, stationary preparation: the population probability of the initially excited electronic state for $\eta = 0.5$, Redfield-theory calculations with the time-dependent Redfield tensor. The increase of the bath temperature suppresses the decay to negative values at longer times.

also for a very strong system-bath coupling, $\eta = 2$ (d), are shown in Fig. 19. The undamped system dynamics (Fig. 19a) is similar to that of the normal region, low-frequency electronic oscillations ($V_{\rm DA} = \omega_0/5 = 0.01$ eV) are superimposed by the higher-frequency vibrations. For the system-bath coupling of η =0.1, Fig. 19b, the electronic oscillations are still present on a ps time scale, competing successfully with the dissipation. The increase of the latter (η =0.5, Fig. 19c) leads to the familiar step structure. As in the other model examples, RT calculations perform very well for η =0.1 and for short-time dynamics in the case of stronger system-bath coupling. At longer times, RT predicts faster population decay compared to

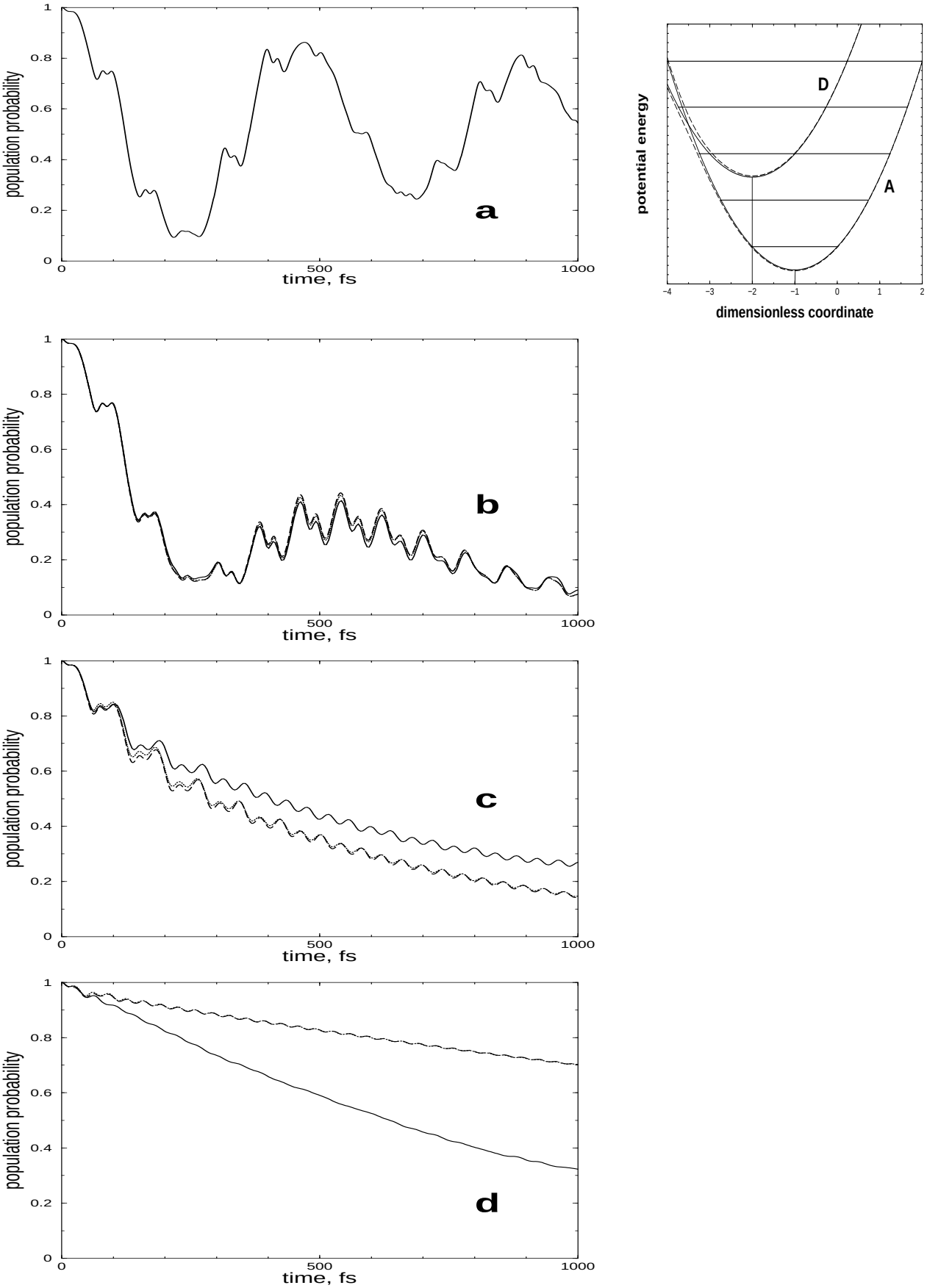

FIG. 19: Inverted region: the population probability of the initially excited electronic state for (a) $\eta = 0$, (b) $\eta = 0.1$, (c) $\eta = 0.5$ and (d) $\eta = 2$. The Redfield results, calculated with the stationary and time-dependent Redfield tensor, are the dashed and dotted curves, respectively. The solid line corresponds to the exact SHA calculations.

the exact results, contrary to the normal-region model (cf. Fig. 19c and Fig. 15c). For the case of a very strong system-bath coupling, $\eta = 2$, the loss in the population is practically structureless (Fig. 19d) and RT breaks down, predicting a far too slow decay.

Long-time deviations in the RT predictions for relative strong system-bath coupling (Figs. 15c, 19d) can be explained as follows. If the damping is rather strong, the long-time ET dynamics is controlled by the barrier height (zero temperature being assumed), as the excess in the vibrational energy (if present) is damped very fast and efficiently. If the renormalization term in the system Hamiltonian is not properly compensated by the imaginary part of the Redfield tensor (as it appears for $\eta = 0.5$, 2), this leads to a change in the effective barrier height and, consequently, to a wrong prediction for the long-time ET-rate.

The stationary Redfield-tensor approximation performs very well in the inverted-region model example. The eigenstate spectrum does possess very small frequencies Ω, which could lead to the slow convergence of the time integrals (34), but the corresponding Redfield tensor elements appear to be very small and the transitions between close-lying levels are negligible.

Generally, the Redfield-theory calculations for the inverted-region model appear to be particularly stable with increase of the system-bath coupling strength. Though there is some discrepancy for the intermediate damping $\eta = 0.5$ (Fig. 19c), the vibrational fine structure at short times and the long-time decay rate are rather well reproduced, whereas in the normal-region examples the same damping strength caused either a wrong prediction for the long-time decay rate (Fig. 15c) or even negative values of the population probability in the limit $t \to \infty$ (Fig. 17c).

6. CONCLUSIONS

A detailed investigation of the modeling of ultrafast ET processes in the condensed phase in the framework of multi-level Redfield-theory has been presented. Redfield theory is based on the system-bath partitioning approach and represents a numerically efficient scheme for the propagation of the reduced density matrix, i.e., for the monitoring of the system dynamics. The perturbative character of the theory with respect to the system-bath coupling restricts possible applications to those reactions where only few degrees of freedom are strongly coupled to the ET, all the other being indirectly involved and thus acting as a weakly coupled dissipative medium.

Models with a single reaction coordinate have been considered throughout this work, although the numerical treatment of up to three system modes is feasible [61]. We have constructed two-electronic-state models for excited-state ET in the normal and inverted regions, and three-electronic-state models for back-ET in the inverted region. The population dynamics of relevant electronic states, as well as the wave-packet motion in these states, have been monitored.

A detailed analysis of the performance of Redfield theory and its common approximations, as well as of the Golden-Rule and diabatic-damping approaches, has been carried out for the class of problems under consideration.

It has been shown that the well-known secular approximation (SA) to Redfield theory exhibits a dramatic breakdown when coherent vibrational motion dominates in the system dynamics, while it is valid for few-level systems with stationary initial conditions. A criterium for the applicability of the SA has been established and the inclusion of the so-called non-strictly secular terms has been proposed as a numerically cheaper alternative to full Redfield-tensor calculations. This alternative can reduce the numerical effort significantly , e.g., for multi-level high-temperature regimes, when many eigenstates have to be included to obtain a converged result.

By performing calculations with both time-dependent and time-independent Redfield

tensor, we have investigated the validity of the stationary Redfield-tensor approximation for different ET models (that is, various system, bath and system-bath coupling parameters). This approximation has been found to be very sensitive to the individual system properties. The common trend observed is its poorer performance for the finite-temperature regime. The improvement of this approximation with decreasing bath correlation time, τ_c, has been illustrated by comparison of time-dependent and time-independent Redfield-tensor results for different values of the cut-off frequency ω_c (the stationary Redfield-tensor approximation would be exact for $\tau_c = 0$, that is, for a δ-form bath correlation functions).

Exploiting the non-perturbative character of Redfield theory with respect to the electronic coupling, we have demonstrated its ability to describe ET beyond the well-known Golden-Rule (nonadiabatic) regime. This has allowed us to reveal the limitations of the Golden-Rule description. With the increase of the electronic coupling, the population back-flow becomes important in the ET dynamics. The Golden-Rule formula does not take into account this effect and thus is able to describe only the initial decay, predicting a too large reaction rate.

The diabatic-damping model for ET has also been tested against the Redfield-theory approach. Its successes and limitations have been outlined and illustrated. As expected, the deviations in the diabatic-damping-model predictions increase with increasing electronic coupling. Nevertheless, the model performs very well for the considered two electronic-state models of ET in the normal and inverted regions. We refer to Ref. [61] and Ref. [62] for further details and examples.

The rotating-wave approximation (RWA), which is assumed in the diabatic-damping model, does not to introduce any significant error in the framework of Redfield theory. It has been found that the effect of the RWA is a reduction of the system-bath coupling.

In the last chapter, we have performed a comparison of multi-level Redfield theory with the numerically exact self-consistent hybrid method, developed by Wang *et al.* [63], in order to reveal the range of validity of the perturbative treatment of the system-bath coupling. The imaginary part of the Redfield tensor has been taken into account in the dissipation description, and the renormalization term has been included in the system Hamiltonian

in order to be consistent with the model of the self-consistent hybrid method. It has been found that Redfield theory is in an excellent agreement with the exact calculations for a weak system-bath coupling strength. With the increase of damping, it reproduces rather well the exact results at short time scales, but at longer times it may predict either a somewhat too fast or too slow ET, and sometimes even negative values for the population dynamics. It has been demonstrated, however, that the decay to negative values disappears for a finite temperature of the bath.

Ultrafast ET, driven by coherent vibrational motion in the excited state, has been studied in the normal and inverted regions within two-electronic state models, applying a nonstationary initial condition. Hence, a moving wave-packet was prepared in the first excited donor state. Wave-packet motion in the acceptor state, appearing during the reaction, has been detected both in the normal and inverted regions. The time scale of the damping of the vibrational motion in the donor and acceptor states has been varied by adjusting the system-bath coupling strength. In the normal region, two principal time scales of the ET have been observed: a very fast initial decay of the donor-state population due to coherent vibrational motion in this state, and a much slower population transfer in the vibrationally relaxed system at longer times due to the tunneling process (zero temperature has been assumed). In the inverted-region model, a significant initial excess in the vibrational energy and a low barrier prevents the vibrational relaxation from slowing down the ET as much as in the normal region.

In the three-state models, a back-ET reaction, occurring via an intermediate bridging state, has been investigated with nonstationary and stationary preparation (i.e., with nonequilibrium and equilibrium nuclear geometry in the initial electronic state at $t = 0$). Wave-packet motion in the ground state has been observed in the both cases, even if there is no moving wave-packet prepared in the first excited state. The wave-packet dynamics with the nonstationary initial condition is similar to that of the two-state model for the inverted region, but the intermediate state delays the transfer to the ground (i.e., acceptor) state. In the case of stationary preparation, the wave-packet motion in the ground state is generated

due to the presence of the intermediate bridging state and is somewhat less coherent than that in the example with the nonstationary initial condition.

An exhaustive study of multi-level Redfield theory for the modeling of ultrafast ET reactions has been presented in this work. The approach has been shown to be an efficient tool for the description of the dynamics of weakly-damped systems and also of the short-time dynamics of systems with a moderate system-bath coupling strength. This, to our knowledge, first systematic investigation of the validity of multi-level Redfield theory for fast ET processes has shown that this numerically cheap approach is reliable for a relatively large range of ET problems. This finding is very promising and motivates, in particular, the application of Redfield theory for theoretical simulations of time-resolved pump-probe spectra of ultrafast ET reactions [102].

APPENDIX A: REPRESENTATIONS OF THE REDUCED DENSITY MATRIX

The Redfield equation (16) employs the system-eigenstate representation (17) of the reduced density matrix (RDM). A direct-product expansion of the system eigenstates

$$|\nu\rangle = \sum_{iv} C_{iv}^{(\nu)} |\phi_i\rangle |v\rangle, \tag{A1}$$

where $|\phi_i\rangle$ are electronic diabatic states and $|v\rangle$ are vibrational harmonic-oscillator states, has been used for the model calculations. The coefficients $C_{iv}^{(\nu)}$ as well as the system eigenenergies E_ν are obtained by diagonalization of the system Hamiltonian (50).

In the absence of dissipation the system can be described either by its wave function $|\Psi\rangle$ or by the density matrix

$$\sigma = |\Psi\rangle\langle\Psi|. \tag{A2}$$

If the system-bath interaction is assumed to be switched on at $t = 0$, the initial RDM in the system-eigenstate representation reads

$$\sigma_{\mu\nu}(t=0) = \langle\mu|\Psi(t=0)\rangle\langle\Psi(t=0)|\nu\rangle,$$

where $|\Psi(t=0)\rangle$ is determined by the initial condition.

To monitor the wave-packet dynamics, the coordinate representation of the RDM

$$\sigma(Q,t) = \sum_{\mu\nu} \sigma_{\mu\nu}(t) \langle Q|\mu\rangle\langle\nu|Q\rangle$$

has been used. Its projection to a certain diabatic electronic state $|\phi_i\rangle$ has been calculated as

$$\langle\phi_i|\sigma(Q,t)|\phi_i\rangle = \sum_{\mu\nu} \sigma_{\mu\nu}(t) \sum_{vv'} C_{iv}^{(\mu)} C_{iv'}^{(\nu)*} \langle Q|v\rangle\langle v'|Q\rangle, \tag{A3}$$

where the harmonic-oscillator eigenfunctions are given by

$$\langle Q|v\rangle = (v!2^v\sqrt{\pi})^{-1/2} H_v(Q) \exp(-Q^2/2).$$

The Hermite polynomials

$$H_v(Q) = (-1)^v \exp(Q^2) \frac{d^v}{dQ^v} \exp(-Q^2)$$

satisfy the recurrence relation

$$QH_v(Q) = vH_{v-1}(Q) + \frac{1}{2} vH_{v+1}(Q).$$

APPENDIX B: NUMERICAL ASPECTS OF REDFIELD-EQUATION SOLUTION

The first task while solving numerically Redfield equation is the diagonalization of the system Hamiltonian. According to the direct product expansion introduced in Apendix A, the H_S-matrix has a dimension $N \times N$ with

$$N = N_e \prod_k^M n_k,$$

where N_e is the number of the relevant diabatic electronic states, M is the number of system modes ($M \equiv 1$ in this work) and n_k is the length of the vibrational (harmonic-oscillator) basis for the kth mode. Standard routines and 8 GB of memory allow the diagonalization of a $N \times N$ matrix for up to $N \sim 10^4$ [61, 82].

The second step is the time-propagation of the reduced density matrix in the system-eigenstate representation. For this purpose, one can safely reduce the eigenstates basis (N) including only the relevant lower states to the propagation. Obviously, the number of these states, N_r, is increasing with the temperature.

At first sight, the numerical effort for the propagation of the RDM according to the Redfield equation seems to scale as N_r^4. But as was shown by Pollard *et al.* [53], the explicit construction of the Redfield tensor can be replaced by a matrix multiplication, which allows to reduce the time-propagation scaling to N_r^3. The efficiency of different numerical propagators for Redfield-equation solving has been discussed in detail in Refs. [54, 103]. In this work we have used a forth-order Runge-Kutta scheme adopted from Ref. [94].

If the Lamb shift is not neglected, the principal-value integration is required, in addition, to constract the Redfield tensor (see eqs. (38), (59)).

Calculations with the time-dependent Redfield tensor are much more expensive compared to those with the stationary tensor, as the time integration is necessary at every time step during the propagation unless the Redfield-tensor elements reach their stationary limit, i.e., for $t \leq \tau_{st}$ (see section 2.4.1).

APPENDIX C: MARCUS CLASSIFICATION OF THE ET REGIONS

According to the Marcus classification [104], one distinguishes between normal and inverted ET regions. The classification is based on the relationship between reorganization energy and free energy difference. In our modeling, the free energy difference corresponds to the adiabatic energy difference of two diabatic potentials, $\varepsilon_{\mathrm{ad}}^{(\mathrm{D})} - \varepsilon_{\mathrm{ad}}^{(\mathrm{A})}$, and the system reorganization energy is defined as $\omega_0/2(\Delta^{(\mathrm{D})} - \Delta^{(\mathrm{A})})^2$. In the normal region, the condition

$$\varepsilon_{\mathrm{ad}}^{(\mathrm{D})} - \varepsilon_{\mathrm{ad}}^{(\mathrm{A})} < \frac{\omega_0}{2}(\Delta^{(\mathrm{D})} - \Delta^{(\mathrm{A})})^2$$

is satisfied, while the opposite relation

$$\varepsilon_{\mathrm{ad}}^{(\mathrm{D})} - \varepsilon_{\mathrm{ad}}^{(\mathrm{A})} > \frac{\omega_0}{2}(\Delta^{(\mathrm{D})} - \Delta^{(\mathrm{A})})^2$$

holds for the inverted region. The situation

$$\varepsilon_{\mathrm{ad}}^{(\mathrm{D})} - \varepsilon_{\mathrm{ad}}^{(\mathrm{A})} = \frac{\omega_0}{2}(\Delta^{(\mathrm{D})} - \Delta^{(\mathrm{A})})^2$$

corresponds to barrierless ET.

REFERENCES

[1] H. Davy, in *Laboratory Notebook* (The Royal Institution Library, London, 1808).

[2] W. Weyl, Poggendorffs Ann. **121**, 601 (1864).

[3] W. Libby, J. Phys. Chem. **67**, 863 (1952).

[4] R. Marcus, J. Chem. Phys. **24**, 966, ibid. 979 (1956).

[5] V. G. Levich and R. R. Dogonadze, Dokl. Acad. Nauk SSSR **78**, 2148 (1959).

[6] N. R. Kestner, J. Logan, and J. Jortner, J. Phys. Chem. **78**, 2148 (1974).

[7] G. Baym, *Lectures on Quantum Mechanics* (Benjamin, Reading, MA, 1973), chap. 12.

[8] J. Jortner and M. Bixon, J. Chem. Phys. **88**, 167 (1988).

[9] H. Sumi and R. A. Marcus, J. Chem. Phys. **84**, 4894 (1986).

[10] K. Yoshihara, K. Tominaga, and Y. Nagasawa, Bull. Chem. Soc. Jpn. **68**, 696 (1995).

[11] E. Åkesson, G. C. Walker, and P. F. Barbara, J. Chem. Phys. **95**, 4188 (1991).

[12] E. Åkesson, A. E. Johnson, N. E. Levinger, G. C. Walker, T. P. DuBruil, and P. F. Barbara, J. Chem. Phys. **96**, 7859 (1992).

[13] G. C. Walker, E. Åkesson, A. E. Johnson, N. E. Levinger, and P. F. Barbara, J. Phys. Chem **96**, 3728 (1992).

[14] N. E. Levinger, A. E. Johnson, G. C. Walker, and P. F. Barbara, Chem. Phys. Lett. **196**, 159 (1992).

[15] A. E. Johnson, N. E. Levinger, W. Jarzeba, R. E. Schlief, and P. F. Barbara, Chem. Phys. **176**, 555 (1993).

[16] G. C. Walker, P. F. Barbara, S. K. Doorn, Y. Dong, and J. T. Hupp, J. Phys. Chem **95**, 5712 (1991).

[17] K. Tominaga, D. A. V. Kilner, A. E. Johnson, N. E. Levinger, and P. F. Barbara, J. Chem Phys. **98**, 1228 (1993).

[18] P. Kambhampati, D. H. Son, T. W. Kee, and P. F. Barbara, J. Phys. Chem. A **104**, 10637 (2000).

[19] D. H. Son, P. Kambhampati, T. W. Kee, and P. F. Barbara, J. Phys. Chem. A **106**,

4591 (2002).

[20] T. Kobayashi, Y. Takagi, H. Kandori, K. K., and K. Yoshihara, Chem. Phys. Lett. **180**, 416 (1991).

[21] H. Kandori, K. K., and K. Yoshihara, J. Phys. Chem. **96**, 8042 (1992).

[22] A. P. Yartsev, Y. Nagasawa, A. Douhal, and K. Yoshihara, Chem. Phys. Lett. **207**, 546 (1993).

[23] Y. Nagasawa, A. P. Yartsev, K. Tominaga, A. E. Johnson, and K. Yoshihara, J. Chem. Phys. **101**, 5717 (1994).

[24] Y. Nagasawa, A. P. Yartsev, K. Tominaga, B. P. B., A. E. Johnson, and K. Yoshihara, J. Phys. Chem. **99**, 653 (1995).

[25] M. Vos, J.-C. Lambry, S. J. Robles, D. C. Youvan, J. Breton, and J.-L. Martin, Proc. Natl. Acad. Sci. USA **88**, 8885 (1991).

[26] W. Zinth, P. Huppmann, T. Arlt, and J. Wachtveitl, Phil. Trans. R. Soc. Lond A **356**, 465 (1998).

[27] K. Wynne, C. Galli, and R. Hochstrasser, J. Chem. Phys. **100**, 4797 (1994).

[28] K. Wynne, G. Reid, and R. Hochstrasser, J. Chem. Phys. **105**, 2287 (1996).

[29] I. Rubtsov and K. Yoshihara, J. Phys. Chem. A **101**, 6138 (1997).

[30] I. V. Rubtsov, H. Shirota, and K. Yoshihara, J. Phys. Chem. A **103**, 1801 (1999).

[31] I. Rubtsov and K. Yoshihara, J. Phys. Chem. A **103**, 10202 (1999).

[32] S. Engleitner, M. Seel, and W. Zinth, J. Phys. Chem. **103**, 3013 (1999).

[33] S. A. Kovalenko, R. Schanz, V. M. Farztdinov, H. Hennig, and N. P. Ernsting, Chem. Phys. Lett. **323**, 312 (2000).

[34] C. Zimmermann, F. Willig, S. Ramakrishna, B. Burfeindt, B. Pettinger, R. Eichberger, and W. Storck, J. Phys. Chem. B **105**, 9245 (2001).

[35] R. Coalson, D. Evans, and A. Nitzan, J. Chem. Phys. **101**, 436 (1994).

[36] P. F. Barbara, G. C. Walker, and T. P. Smith, Science **256**, 975 (1992).

[37] U. Weiss, *Quantum Dissipative Systems* (World Scientific, Singapore, 1999), 2nd ed.

[38] W. H. Louisell, *Quantum Statistical Properties of Radiation* (Wiley, New York, 1973).

[39] K. Blum, *Density Matrix Theory and Applications* (Plenum, New York, 1981).

[40] A. J. Leggett, S. Chakravarty, A. T. Dorsey, M. P. A. Fisher, A. Garg, and W. Zwerger, Rev. Mod. Phys. **59**, 1 (1987).

[41] R. D. Coalson, J. Chem. Phys. **86**, 995 (1987).

[42] C. H. Mark and D. Chandler, Phys. Rev. A **44**, 2352 (1991).

[43] N. Makri and D. E. Makarov, J. Chem. Phys. **102**, 4600 (1995).

[44] N. Makri, J. Phys. Chem. A **102**, 4414 (1998).

[45] Y. Toyozawa and M. Inoue, J. Phys. Soc. Jpn. **21**, 1663 (1966).

[46] T. Takagahara, E. Hanamura, and R. Kubo, J. Phys. Soc. Jpn. **44**, 728 (1978).

[47] D. Makarov and N. Makri, Phys. Rev. A **48**, 3626 (1993).

[48] J. M. Jean, R. A. Friesner, and G. R. Fleming, J. Chem. Phys. **96**, 5827 (1992).

[49] A. G. Redfield, Adv. Magn. Reson. **1**, 1 (1965).

[50] V. May, O. Kühn, and M. Schreiber, J. Phys. Chem. **97**, 12591 (1993).

[51] B. Wolfseder and W. Domcke, Chem. Phys. Lett. **235**, 370 (1995).

[52] B. Wolfseder and W. Domcke, Chem. Phys. Lett. **259**, 113 (1996).

[53] W. T. Pollard and R. A. Friesner, J. Chem. Phys. **100**, 5054 (1994).

[54] W. T. Pollard, A. Y. Felts, and R. A. Friesner, Adv. Chem. Phys. **XCIII**, 77 (1996).

[55] G. Lindblad, Commun. Math. Phys. **48**, 119 (1976).

[56] J. Dalibard, Y. Castin, and K. Mølmer, Phys. Rev. Lett. **68**, 580 (1992).

[57] A. K. Felts, W. T. Pollard, and R. A. Friesner, J. Phys. Chem. **99**, 2929 (1995).

[58] J. Jean, J. Phys. Chem. A **102**, 7549 (1998).

[59] B. Wolfseder, L. Seidner, G. Stock, and W. Domcke, Chem. Phys. **217**, 275 (1997).

[60] B. Wolfseder, L. Seidner, G. Stock, W. Domcke, M. Seel, S. Engleitner, and W.Zinth, Chem. Phys. **233**, 323 (1998).

[61] D. Egorova, A. Kühl, and W. Domcke, Chem. Phys. **268**, 105 (2001).

[62] U. Kleinkathöfer, I. Kondov, and M. Schreiber, Chem. Phys. **268**, 121 (2001).

[63] H. Wang, M. Thoss, and W. H. Miller, J. Chem. Phys. **115**, 2979 (2001).

[64] C. Meier and D. Tanoor, J. Chem. Phys. **111**, 3365 (1999).

[65] L. Hartmann, I. Goychuk, M. Grifoni, and P. Hängi, Phys. Rev. E **61**, 4687 (2000).

[66] M. Thoss, H. Wang, and W. H. Miller, J. Chem. Phys. **115**, 2991 (2001).

[67] S. Nakajima, Progr. Theor. Phys. **20**, 948 (1958).

[68] R. Zwanzig, J. Chem. Phys. **33**, 1338 (1960).

[69] V. Romero-Rochin and I. Oppenheim, Physica A **155**, 57 (1989).

[70] V. May and M. Schreiber, Phys. Rev. A **45**, 2868 (1992).

[71] D. Kohen, C. C. Marston, and D. J. Tannor, J. Chem. Phys. **107**, 5236 (1997).

[72] P. Gaspard and M. Nagaoka, J. Chem. Phys. **111**, 5676 (1999).

[73] T. Mančal and V. May, J. Chem. Phys. **114**, 1510 (2001).

[74] C. Cohen-Tannoudji, *Frontiers in Laser Spectroscopy* (North Holland, Amsterdam, 1975), vol. I.

[75] D. Evans and R. Coalson, J. Chem. Phys. **104**, 3598 (1996).

[76] K. Ando and H. Sumi, J. Phys. Chem. B **102**, 10991 (1998).

[77] A. Kühl and W. Domcke, Chem. Phys. **259**, 227 (2000).

[78] O. Kühn, V. May, and M. Schreiber, J. Chem. Phys. **101**, 10404 (1994).

[79] J. Jean, J. Chem. Phys. **104**, 5638 (1996).

[80] A. Matro and J. A. Cina, J. Phys. Chem. **99**, 2568 (1995).

[81] D. Segal, A. Nitzan, W. Davis, M. Wasielewsky, and M. Ratner, J. Phys. Chem. B **104**, 3817 (2000).

[82] A. Kühl and W. Domcke, J. Chem. Phys. **116**, 263 (2002).

[83] S. Hahn and G. Stock, J. Chem. Phys. **116**, 1085 (2002).

[84] W. Lichten, Phys. Rev. **131**, 229 (1963).

[85] F. Smith, Phys. Rev. **179**, 111 (1969).

[86] M. Baer, Chem. Phys. **15**, 49 (1976).

[87] W. Domcke and G. Stock, Adv. Chem. Phys. **100**, 1 (1997).

[88] C. Kalyanaraman and D. Evans, J. Chem. Phys. **115**, 7076 (2001).

[89] M. Thoss, *Modellierung dissipativer Prozesse in Rydbergzuständen großer Moleküle ...*, Ph.D. thesis, Technische Universität München (1998).

[90] P. Barbara, T. Meyer, and M. Ratner, J. Phys. Chem. **100**, 13148 (1996).

[91] J. Jortner and M. Bixon, eds., *Electron Transfer: From Isolated Molecules to Biomolecules*, vol. 107 of *Advanced in Chemical Physics* (John Wiley & Sons, Inc., 1999).

[92] S. Fischer and R. Van Duyne, Chem. Phys. **26**, 9 (1977).

[93] G. Lang, E. Paladino, and U. Weiss, Chem. Phys. **244**, 111 (1999).

[94] W. Press, S. Teukolsky, W. Vetterling, and B. Flannery, *Numerical Recipes in Fortran – The Art of Scientific Computing* (Cambridge University Press, Cambridge, 1992), 2nd ed., (NM).

[95] L. Allen and J. Eberly, *Optical Resonance and Two-Level Atoms* (Dover, New York, 1987).

[96] D. Evans and R. Coalson, J. Chem. Phys. **102**, 5658 (1995).

[97] D. Evans, A. Nitzan, and M. Ratner, J. Chem. Phys. **108**, 6387 (1998).

[98] M. Thoss and H. Wang, Chem. Phys. Lett. **358**, 298 (2002).

[99] H.-D. Meyer, U. Manthe, and L. S. Cederbaum, Chem. Phys. Lett. **165**, 73 (1990).

[100] U. Manthe, H.-D. Meyer, and L. S. Cederbaum, J. Chem. Phys. **97**, 3199 (1992).

[101] M. H. Beck, A. Jäckle, G. A. Worth, and H.-D. Meyer, Phys. Rep. **324**, 1 (2000).

[102] S. Mukamel, *Principles of Nonlinear Optical Spectroscopy* (University Press, Oxford, 1995).

[103] I. Kondov, U. Kleinkathöfer, and M. Schreiber, J. Chem. Phys. **114**, 1497 (2001).

[104] R. Marcus, Discuss. Faraday Soc. **29**, 21 (1960).

This work has appeared thanks to Prof. Dr. A.K. Belyaev, Prof. Dr. W. Domcke, Dr. M. Thoss.

I am very grateful to Prof. Dr. Wolfgang Domcke for his wonderful supervising and invaluable help at every stage of my PhD studies.

I was happy to meet and enjoy to work with Dr. Michael Thoss, whose professionalism and support are so encouraging.

Sincere thanks to Prof. Dr. Achim Großer for my first scientific experience.

I would like also to thank everyone I worked with at the University of Dusseldorf and at the Technical University of Munich. In particular, Ms. Karin Schuck for her helpfulness, Dr. Ralph Gillen for his care, Dr. Bojana Ostojic for her sympathy, Dr. Fermin Huarte for his cordiality, Dr. Maxim Gelin for his believing in me. I am also grateful to Lena Philippova and to the Russian-speaking community of the "Forschungsgelände" in Garching for adorning the non-scientific part of my life. In particular, to Dmitrij Ganyushin, Alexei Matveev and Nikita Ter-Oganessian for their help.

Very special thanks to my mother for her patience and for her love.